Acta Biomaterialia 196 (2025) 93–108

Contents lists available at ScienceDirect

Acta Biomaterialia

journal homepage: www.elsevier.com/locate/actbio

Full length article

Inflammation-modulating elastic decellularized extracellular matrix scaffold promotes meniscus regeneration

Yangfan Ding [a,1], Moran Huang [b,1], Pengfei Cai [a,c], Xiao Yu [a], Jie Cui [a], Binbin Sun [a], Xiumei Mo [a], Changrui Lu [a,*], Jiwu Chen [b,**], Jinglei Wu [a,*]

[a] Shanghai Engineering Research Center of Nano-Biomaterials and Regenerative Medicine, College of Biological Science and Medical Engineering, Department of Biomedical Engineering, Donghua University, Shanghai 201620, China
[b] Department of Sports Medicine, Shanghai General Hospital, Shanghai Jiao Tong University School of Medicine, Shanghai 200080, China
[c] G.E.R.N. Research Center for Tissue Replacement, Regeneration & Neogenesis, Department of Orthopedics and Trauma Surgery, Faculty of Medicine, Medical Center-Albert-Ludwigs-University of Freiburg, 79085 Freiburg im Breisgau, Germany

ARTICLE INFO

Keywords:
Decellularized extracellular matrix
Scaffold
Anti-inflammatory
Meniscus regeneration

ABSTRACT

Scaffold-guided meniscus repair and regeneration show promise for meniscus injuries. Desirable scaffold properties are key to promoting proper tissue remodeling and effective regeneration. Herein, we report an inflammation-modulating elastic decellularized extracellular matrix (ECM) scaffold and evaluate its biological performance on meniscus repair in a rabbit model. An elastic scaffold of decellularized meniscus ECM (dmECM) was first prepared and functionalized with chitosan (CS) and ibuprofen (IBU) to obtain dmECM/CS-IBU scaffold. Our results show that CS and IBU grafting did not affect the overall properties of the dmECM/CS-IBU scaffold, including porous structure, good mechanical strength and elasticity. It promoted chondrocyte proliferation and preserved chondrogenic properties. In addition, both *in vitro* and *in vivo* assessments indicate that the dmECM/CS-IBU scaffold showed good anti-inflammatory properties and promoted pro-healing polarization of macrophages. In a partial rabbit meniscus defect model, the dmECM/CS-IBU scaffold showed promotive effects on *in situ* meniscus repair and preserved cartilage tissue. Therefore, our study provides a feasible strategy for fabricating scaffolds with tissue-specific bioactivity and inflammation-modulating abilities that synergistically promote meniscus repair and regeneration.

Statement of significance: Desirable scaffold properties are key to promoting proper tissue remodeling and effective regeneration of meniscus injuries. Herein, elastic decellularized scaffolds were prepared using natural meniscus and successfully grafted with chitosan and the anti-inflammatory drug ibuprofen (dmECM/CS-IBU). The dmECM/CS-IBU scaffold showed a pro-proliferative and phenotype- preserving effect on chondrocytes. In both *in vitro* and *in vivo* models, dmECM/CS-IBU scaffolds exhibited wonderful anti-inflammatory activity. In a meniscus white zone defect model, the dmECM/CS-IBU scaffold demonstrated *in situ* repair of tissue and protection of cartilage tissue. Therefore, we provides a feasible strategy for fabricating scaffolds with tissue-specific bioactivity and inflammation-modulating abilities that synergistically promote meniscus repair and regeneration.

1. Introduction

The meniscus is a pair of crescent-shaped wedges of fibrocartilage tissue that plays a critical role in maintaining the normal function of knee joints. Because meniscal lesions occur particularly in the inner region where vascularization is lacking, the meniscus shows an extremely limited self-healing capacity. Partial or total meniscectomy was once prevalently used to treat meniscus injuries but it was found to cause impaired stress concentrations and load transfer disorders in the knee joint, finally leading to osteoarthritis (OA) [1]. Recently, grafts

* Corresponding authors at: Department of Biomedical Engineering, Donghua University, Shanghai 201620, China.
** Corresponding author at: Shanghai Engineering Research Center of Nano-Biomaterials and Regenerative Medicine, College of Biological Science and Medical Engineering, Department of Biomedical Engineering, Donghua University, Shanghai 201620, China.
E-mail addresses: crlu@dhu.edu.cn (C. Lu), jeevechen@gmail.com (J. Chen), jw@dhu.edu.cn (J. Wu).
[1] These authors contributed equally to this study.

https://doi.org/10.1016/j.actbio.2025.02.043
Received 8 October 2024; Received in revised form 31 January 2025; Accepted 20 February 2025
Available online 21 February 2025

have gained increasing attention for meniscus repair. In the case of meniscus transplantation, the most critical problems are lack of donor, infection, anatomical mismatch, and immune rejection [2]. Current meniscus implants, such as collagen meniscus implants (CMI), have been widely used. Despite the positive short-term results, few treatments have yielded long-term functional meniscal tissue regeneration [3]. Long-term studies have reported sustained remodeling of CMI scaffolds, but only 15–20% of patients completely resorb the CMI [4]. In addition, studies have found that CMI has not demonstrated a cartilage-protecting effect at up to 20 years follow-up [5].

Biological scaffolds of extracellular matrix (ECM) materials originating from various tissues/organs have been demonstrated to promote tissue healing and repair, showing great promise in preclinical animal studies and human clinical trials [6]. Decellularized meniscus ECM (dmECM) scaffolds have been efforted for meniscus repair and regeneration due to their tissue-specific biological cues, biomimetic structure, and biomechanical properties [7]. Recently, our group has developed a series of dmECM materials derived from porcine meniscus, which have been proved to have advantages in terms of decellularization efficiency and biocompatibility [8–12]. We found that effective removal of DNA contributed to a milder acute inflammation for the dmECM scaffold. However, considerable foreign body response (FBR) was observed when dmECM porous scaffold was subcutaneously implanted in rats in our previous study [11]. Early host immune response caused by xenogeneic decellularized materials during implantation is a concern, which may become an obstacle to successful implantation [13]. Host response to dmECM scaffolds involves both the innate and acquired immune systems. Once dmECM is implanted, a cellular response consisting mainly of macrophages takes place. Studies have shown that macrophages act as a double-edged sword, playing both positive and negative roles in the constructive remodeling of wounds [14].

Macrophages are key immune cells and the first line of external defense of the body's innate immune system. In response to injury or external invasion of the body, macrophages are stimulated by inflammatory chemotactic signals and rapidly migrate to the site of inflammation to initiate an immune response [15]. Macrophages can be broadly described as having an M1 phenotype, which is responsible for the initial acute inflammatory reaction, and an M2 phenotype during the later remodeling phases of wound healing and fibrous capsule formation [16]. An abnormal M1-to-M2 ratio of macrophages is likely to cause the failure of decellularized ECM implantation. Thus, it is critical to modulate the M1 response to foreign bodies and induce an early transition to the M2 phenotype [17]. Non-steroidal anti-inflammatory drugs (NSAIDs), such as ibuprofen (IBU), are commonly used to treat pain and inflammation [18]. However, the poor water solubility of IBU leads to its low delivery efficiency. Meanwhile oral delivery of IBU may lead to mild to moderate side effects, including gastrointestinal ulcers, gastric bleeding, and perforation, as well as serious consequences of heart and kidney damage [19]. It is necessary to improve the efficiency of IBU delivery as well as to change the mode of delivery to minimize side effects while exerting its effects. Chitosan (CS) is a natural polysaccharide with good biocompatibility, biodegradability, and moderate anti-inflammatory as well as antibacterial abilities, which is widely used in tissue engineering scaffolds [20]. Because CS carries abundant amino groups and shows nucleophilic behavior, it is easy to be chemically modified or functionalized to improve biomaterials [21]. Therefore, CS is often used together with other polymers in tissue engineering applications. In this study, we searched for a suitable method to combine dmECM with small molecule drugs with anti-inflammatory capacity.

In this study, an inflammation-modulating scaffold was designed by functionalizing dmECM with CS and IBU, which not only possessed tissue-specific bioactivity but also had appropriate mechanical and anti-inflammatory properties. Briefly, according to Scheme 1, we first prepared dmECM powders by cyclic freeze-thaw grinding with DNase treatment and freeze-drying to obtain scaffolds of appropriate size. After pre-crosslinking by dehydrothermal treatment to improve structural stability, CS and IBU were then grafted onto scaffolds via carbodiimide chemistry. We comprehensively characterized the physicochemical properties of the dmECM/CS-IBU scaffold, including morphology, composition, mechanical properties, and IBU release. Cytocompatibility and anti-inflammatory capacity of the scaffold were evaluated *in vitro* and *in vivo*. Finally, the scaffold was applied to white zone meniscus

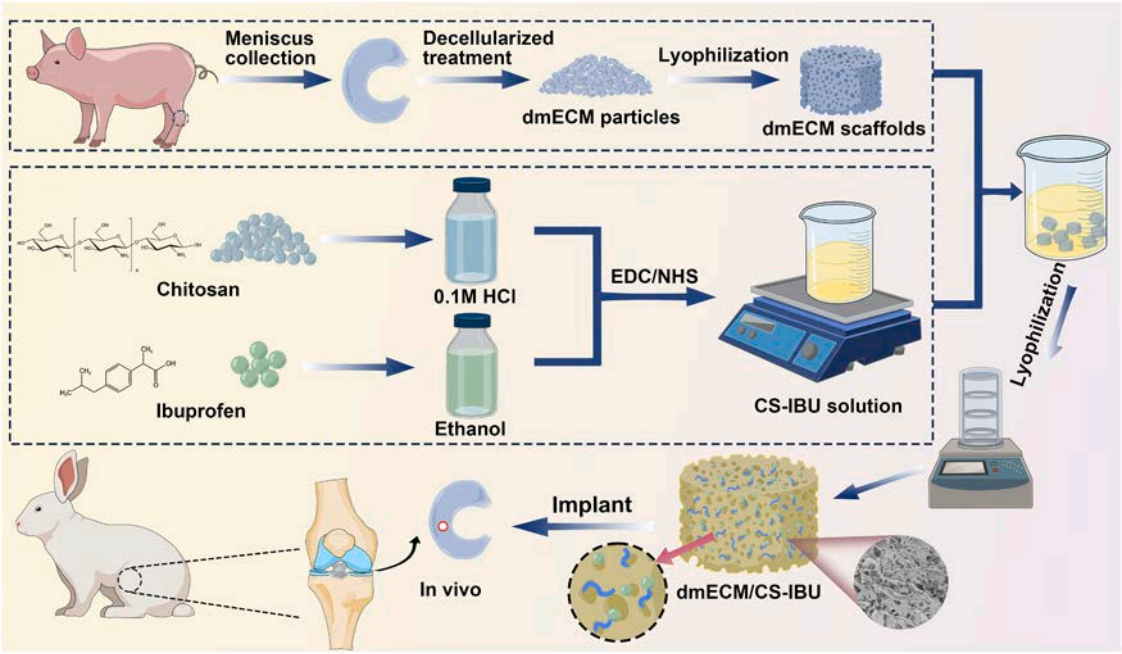

Scheme 1. Schematic diagram of the preparation process of meniscus decellularized extracellular matrix scaffold grafted with CS as well as IBU (dmECM/CS-IBU). The dmECM scaffolds were first prepared by the method of cyclic freeze-thaw milling. CS and IBU were dissolved separately and activated by adding EDC/NHS, and then the dmECM scaffolds were immersed into the CS-IBU solution for reaction. The dmECM/CS-IBU scaffolds grafted with CS-IBU were produced by water washing and lyophilization, and the bioactivity of the scaffolds was evaluated *in situ*.

defect in rabbits to determine its biological performance on meniscus repair and cartilage preservation.

2. Materials and methods

2.1. Materials

DNase, chitosan, and ibuprofen were obtained from Macklin Inc., Shanghai, China. Magnesium chloride, bovine serum albumin (BSA), and lipopolysaccharide (LPS) were purchased from Sigma-Aldrich. 1-(3-dimethylaminopropyl)-3-ethylcarbodiimide hydrochloride (EDC), N-hydroxysuccinimide (NHS), Hydrochloride acid and 200-proof ethanol were supplied by Sinopharm Chemical Reagent Co., Ltd. Trizol, Triton X-100, phalloidin, and DAPI were purchased from Beyotime, Shanghai, China.

2.2. Preparation of dmECM/CS-IBU scaffolds

The preparation of the dmECM scaffold and subsequent functionalization with CS and IBU is shown in Scheme 1. The dmECM particle and scaffolds were prepared following our previous study [11]. Briefly, cyclic freeze-thaw grinding treatment was performed using a soybean grinder (JYL – C022E, Joyoung Co. Ltd.), with each grinding for approximately 30 s at room temperature. After about a 20 grinding process, fine powders (~ 50 μm) on the wall of the grinder were collected, and the remaining meniscus was continued in a continuous grinding process. Meniscus powders were treated with 20 KU/ml DNase in 50 mM magnesium chloride for 2 h at 37 ℃, thoroughly washed with deionized water, and then centrifuged at 6000 rpm for 10 min. The obtained dmECM slurry was transferred into a mold for freeze-drying and heating treatment at 120 ℃ for 12 h to fabricate pre-crosslinked dmECM scaffolds.

For functionalization, CS was dissolved in 0.1 M hydrochloric acid and IBU was dissolved in anhydrous ethanol and the carboxyl group was activated with EDC to form O-acetylsalicylic acid intermediate, and then replaced the O-acetylsalicylic acid group with NHS (N-hydroxysuccinimide) to form IBU-NHS intermediate. Slowly add the IBU-NHS intermediate product to the CS solution to form a homogeneous solution. Then, the pre-crosslinking dmECM scaffold was immersed in CS-IBU solution and shaken gently overnight at room temperature. Subsequently, the scaffolds were taken out, deacidified with 90% ethanol, rinsed repeatedly with a large amount of deionized water, and lyophilized to obtain dmECM/CS-IBU scaffolds. The concentrations of CS and IBU are listed in Table S1.

2.3. Characterization of dmECM/CS-IBU scaffolds

Histological analyses of native meniscus and dmECM were performed, including hematoxylin & eosin (H&E), Alcian blue, and DAPI. Biochemical compositions of cellular double-stranded DNA (dsDNA), collagen, and sulfate glycosaminoglycan (sGAG) were determined by Genomic DNA Extraction Kit (Beyotime), hydroxyproline assay (Nanjing Jiancheng), and 1,9-dimethylmethylene blue (DMMB) assay, respectively [11] (n = 6).

Gross appearance of scaffolds was photographed with a digital camera. The morphology of scaffolds was observed by scanning electron microscopy (SEM). Samples were sputter-coated with gold and imaged under a Phenom XL desktop scanning electron microscope (Phenom, Netherlands) at an accelerating voltage of 5 kV.

The porosity and density of scaffolds were determined by a liquid displacement method as described previously [22]. Briefly, the diameters (d) and heights (h) of the cylindrical scaffolds were measured and the dry sample was weighed (m_0) and then immersed in ethanol (200-proof) for 1 h. Scaffolds were retrieved from ethanol and weighed (m_1). The scaffold porosity was calculated by the following equation: $porosity\ (\%) = \frac{100 \times (m_1 - m_0)}{\rho_{ethanol} \times (d/2)^2 \times h \times \pi}$. The density of scaffold was calculated using the following equation: $\rho = \frac{m_0}{(d/2)^2 \times h \times \pi}$. Five replicates were measured for each scaffold. Pore sizes of scaffolds were measured from SEM images using Image J (n = 5).

Compositional analysis was conducted by Fourier transform infrared spectroscopy (FTIR). Scaffolds were analyzed using an attenuated total FTIR (Nicolet-6700, Thermo Fisher, USA) over the range of 500–4000 cm^{-1}. The thermogravimetric analysis of scaffolds was performed using a Thermogravimetric Analyzer (PerkinElmer Enterprise Management (Shanghai) Co., Ltd., TGA8000, Shanghai, China). The process was carried out at a heating rate of 5 °C/min from room temperature to 800 °C. The thermogravimetric parameters were analyzed by the TGA curves [23]. The crystalline phase of scaffolds was analyzed by an X-ray diffractometer (XRD, D8 Discover, Bruker AXS, Billerica, MA).

The volume expansion ratio and water absorption capacity of scaffolds were assessed according to our previous report [24,25]. The diameter (d_0), height (h_0), and mass (m_d) of dry samples were measured. The samples were incubated in deionized water for certain periods. Wet samples were gently wiped using tissue paper and weighed (m_w) at different time points. The diameter (d_1) and height (h_1) were measured when the maximum water absorption was reached. Volume expansion ratio was calculated by the following equation: $Volume\ expantion\ ratio\ (\%) = \frac{(d_1/2)^2 \times h_1 \times \pi - (d_0/2)^2 \times h_0 \times \pi}{(d_0/2)^2 \times h_0 \times \pi} \times 100\%$. Water absorption capacity was calculated using the following equation: $Water\ absorption\ capacity\ (\%) = \frac{m_w - m_d}{m_d} \times 100\%$. Five replicates were measured for each scaffold.

Degradation and drug release of the scaffolds were measured following our previous report [12,26]. Dry scaffolds were cut into pieces (~ 10 mg/piece) and weighed (m_0, n = 3). The scaffolds were incubated in 2 mL of phosphate buffered saline (PBS) at 37 ℃, 100 rpm. The scaffolds were then harvested, lyophilized, and weighed after 7, 14, and 21 days (m_1). Mass remaining of scaffolds was calculated by the following equation: $Mass\ remaining\ (\%) = \left(1 - \frac{m_0 - m_1}{m_0}\right) \times 100\%$. Images of the microstructure of scaffolds after 21 days of degradation were taken with SEM. IBU (10 mg) was weighed and different concentration gradients of IBU solution were prepared. The absorbance values of IBU solution were detected by an Ultraviolet spectrophotometer (TU-1810) at 264 nm and the standard curve was plotted. The absorbance values were measured from the supernatant of the degraded samples at days 1, 3, 9, 14, 21, and 30 to analyze the release of IBU (n = 6).

Compression properties of scaffolds were tested using a universal material testing machine with a 50 N load cell (Instron 5567, Norwood, MA). Scaffolds were incubated in PBS overnight before test. Unconfined uniaxial compression was performed at a constant crosshead speed of 3 mm/min until failure. The breaking strain was read from the stress-strain curve and the corresponding stress was read as the compressive strength (n = 5). The compression modulus was calculated from the first 20% of the strain in the linear region of the compression stress-strain curve (n = 5). To determine the elastic properties of scaffolds, a 100-cycle compression test was performed at the compressing speed of 5 mm/min. Samples were tested at various maximum load strains of 30%. Compression strength and compressive modulus after every 10 cycles were calculated and normalized to those of the first cycle to determine mechanical loss during the cyclic compression test.

2.4. Cytocompatibility of dmECM/CS-IBU scaffolds

Primary bone marrow mesenchymal stem cells (BMSCs) and articular chondrocytes were isolated from Sprague-Dawley (SD) rats according to our previous report [11,27]. BMSCs and chondrocytes between passages 2 (P_2) and 4 (P_4) were used. NIH 3T3 fibroblasts and RAW 264.7 macrophages were obtained from the Cell Bank of the Chinese Academy of Sciences and were expanded for cell study. All the cells

were maintained and expanded in high glucose Dulbecco's Modified Eagle medium (DMEM) supplemented with 10% fetal bovine serum and 1% penicillin/streptomycin antibiotics at 37 ℃, 5% CO_2. The medium was refreshed every 2 days.

Scaffolds (10 mm diameter, 2 mm height) were sterilized by UV irradiation. NIH 3T3 fibroblasts were seeded on the scaffolds with 2×10^5 cells per scaffold and cultured in complete medium. The proliferation of cells was determined by the Cell Counting Kit-8 (CCK-8) assay analysis (n = 6) and the absorbance was measured at 450 nm using a microplate reader (Multiskan MK3, Thermo Fisher Scientific). Fibroblasts on the scaffolds were stained with live/dead assay and imaged with a fluorescence microscope (DMi 8, Leica, Germany). Cell-seeded scaffolds were fixed with 4% paraformaldehyde (PFA), dehydrated with a gradient alcohol, and then imaged with SEM.

The scaffold extracts were prepared following the international standard ISO 10,993 for further experiments. BMSCs were cultured using scaffold conditioned medium, and the CCK-8 (n = 6) and live/dead assay were performed to assess the cytotoxicity of scaffolds.

2.5. Evaluation of chondrogenesis preservation in vitro

Chondrocytes were seeded on the scaffolds with 2×10^5 cells per scaffold, stained with live/dead assay, and imaged with a fluorescence microscope at days 7 and 14. At day 7, chondrocyte-seeded scaffolds were fixed with 4% PFA, permeabilized with 0.1% Triton X-100, and blocked with 5% BSA, incubated with rabbit polyclonal antibody Coll II (1:300, Proteintech, USA) followed by the Alexa Fluor 488 goat anti-rabbit IgG H&L (1:500, Beyotime, China). After washing with PBS, the cytoskeleton and nucleus of chondrocytes were labeled with Actin-Tracker Red-594 (1:500, Beyotime, China) and DAPI, respectively. The chondrocytes were imaged with a fluorescence microscope, and the positive area of Coll II was quantified by Image J.

Chondrocytes were seeded in 48-well plates at 2.0×10^5 cells/well and replaced with equal volumes of scaffold extract medium after 1 day. Cells on days 7 and 14 were fixed with 4% PFA. Alcian blue staining (C0153S, Beyotime Biotechnology, Shanghai, China) solution was added to each well and the cells were imaged with an inverted microscope. The positive density was measured with Image J (n = 5). Chondrocytes were seeded in 6-well plates at 5.0×10^5 cells/well and cultured for up to 24 h for cell scratching experiment. A scratch was created using a 200 μL pipette tip, and then equal volumes of low-serum scaffold extract medium were added. The scratches were imaged with an optical microscope (BX53–3M50, AOSVI, Shenzhen, China) after culturing for 0, 12, 24, and 48 h. The migration areas of the same parts were calculated using Image J (n = 7). GAG and collagen levels of chondrocytes were quantified after 7 days as described in a previous study [12] (n = 6). Recombinant Type I collagen (C01–02SC, Trautec, Jiangsu) was introduced as a positive control.

Expression of genes (*Col1α1, Col2α1, SOX9, Aggrecan*) was analyzed by RT-qPCR, and the primer sequences were listed in Table S2. Total RNA was extracted from chondrocytes cultured on the scaffolds at days 7 and 14 (n = 4) with Trizol and cDNA was synthesized using RevertAid First Strand cDNA Synthesis kit (Thermo Fisher Scientific) according to instructions. RT-qPCR was performed on an Applied Biosystems™ 7500 real-time PCR system using NovoStart® SYBR qPCR SuperMix Plus (Novoprotein Scientific Inc., China) and analyzed by comparative Ct quantification method (ΔΔCt).

2.6. Assessment of anti-inflammatory capacity

RAW 264.7 macrophages were seeded on the dmECM/CS-IBU scaffolds with 2×10^5 cells per scaffold. Macrophages on the scaffolds were stained with live/dead assay and imaged with a fluorescence microscope after 48 h.

Macrophages were seeded in 6-well plates at 3.0×10^6 cells/well and cultured in complete medium for 24 h and then stimulated by complete medium containing 100 ng/ml LPS for 12 h [28]. Next, equal volumes of scaffold extract medium were added. Macrophages without stimulation were used as the control in all experiments.

Macrophages were marked with anti-mouse CD86 antibody and CD206 antibody, and measured with flow cytometry [29]. Briefly, LPS-induced macrophages cultured for 24 h were collected and incubated with CD86 (FITC conjugated, Proteintech, China) and CD206 (PE-Cyanine5 conjugated, Biolegend, USA) for 30 min, and then cells were measured with a flow cytometer (FACS Calibur, Becton Dickinson, Franklin Lakes, NJ, USA) and FlowJo software (n = 3). Reactive oxygen species (ROS) level was detected using dichlorofluorescein diacetate assay (Beyotime Biotechnology, Shanghai, China). Cells cultured for 24 h were labeled with 10 μM DCFH-DA for 30 min at 37 °C, followed by incubating with 4′,6-diamidino-2-phenylindole (DAPI) for 5 min at room temperature in dark. Samples were washed with PBS three times and observed by fluorescence microscope (DMi 8, Leica, Germany). ROS level was analyzed by Image J (n = 3) [30]. Nitrite accumulated in the culture supernatant was determined as an indicator of nitric oxide (NO) production by the Griess reagent (Beyotime Biotechnology, Shanghai, China). The cell supernatant cultured for 24 h was collected and then incubated with Griess reagent following the protocol. The absorbance at 540 nm was measured in a microplate reader (Multiskan MK3, Thermo, USA) (n = 3). The amount of nitrite was quantified using a sodium nitrite standard curve. Gene expression (*IL-6, IL-1β, IL-10*) of LPS-induced cells was quantified using RT-qPCR as in Section 2.5, and the primer sequences were listed in Table S3.

2.7. In vivo evaluation

Animal experiments were reviewed and approved by the Animal Care and Use of Shanghai General Hospital (2022AW032).

A rat subcutaneous implantation model was used to assess the role of dmECM/CS-IBU scaffolds for inflammatory modulation as described in previous studies [11]. Briefly, incisions were made in the back of the rat and a subcutaneous pocket was formed by blunt dissection. The scaffolds (dmECM, dmECM/CS, dmECM/CS-IBU) were implanted and then carefully sutured (n = 3). Samples were collected from rats executed 7 days after surgery, fixed in 4% PFA, and paraffin-embedded. For histological analysis, samples were stained for H&E and Masson staining using standard protocols. Immunohistochemical analysis was performed to determine macrophage polarization in response to various scaffolds. Sections were stained using rabbit anti-CD11b (Abcam) and anti-CD206 (Abcam) followed by incubation with horseradish peroxidase-conjugated goat anti-rabbit secondary antibody (Jackson ImmunoResearch Laboratories). Sections were imaged under a light microscope. Immunofluorescence staining was performed for more precise differentiation of immune cell subsets. Sections were incubated with anti-CD45, anti-CD3, anti-MPO, and anti-CD68 primary antibodies. After incubation with biotinylated secondary antibodies, sections were used and imaged under fluorescence microscope. The area of positive cells was counted using Image J (n = 3).

A rabbit meniscus defect model was constructed to validate the ability of the scaffolds to repair meniscus injuries. Fifteen male New Zealand rabbits were used in this experiment and were randomly divided into three groups (n=5): the empty control (control), the dmECM group, and the dmECM/CS-IBU group. The specific surgical procedures were as follows: before surgery, the rabbits were anesthetized with isoflurane inhalation. Subsequently, the right knee joint of each rabbit was exposed through a medial patellar incision, and a 1.5 mm cylindrical defect was created in the medial two-thirds of the anterior horn of the medial meniscus. The empty control group received no treatment, while the dmECM group and the dmECM/CS-IBU group had the corresponding scaffolds placed at the defect site. The wound was then closed layer by layer, and penicillin was administered to prevent infection. The native meniscus was taken from the other unoperated joint (native meniscus). After three months, the rabbits were executed

and the menisci and joints were obtained for further analysis. For histological analysis, samples were stained for H&E, Toluidine blue, and Safranin O staining using standard protocols. The expression of type I collagen and type II collagen was detected with immunohistochemical analysis. Sections were stained using rabbit polyclonal antibody (Abcam) followed by incubation with horseradish peroxidase-conjugated goat anti-rabbit secondary antibody (Servicebio, China). Sections were imaged under a light microscope.

The cartilage of the femur and tibia was macroscopically assessed using the International Cartilage Repair Society (ICRS) classification [31]. Subsequently, the femur and tibia were fixed in 10% (v/v) neutral buffered formalin and decalcified with 10% EDTA to complete the histological assessment. After one and a half months of decalcification, the femur and tibia were prepared for sectioning and stained with H&E and toluidine blue.

2.8. Statistical analysis

Data are presented as mean ± standard deviation. Statistical analysis was performed by one-way analysis of variance (ANOVA) with Tukey's post hoc multiple comparisons. A p-value less than 0.05 was considered statistically significant.

3. Results

3.1. Properties of dmECM/CS-IBU scaffolds

The dmECM powders were prepared by cyclic freeze-thaw grinding

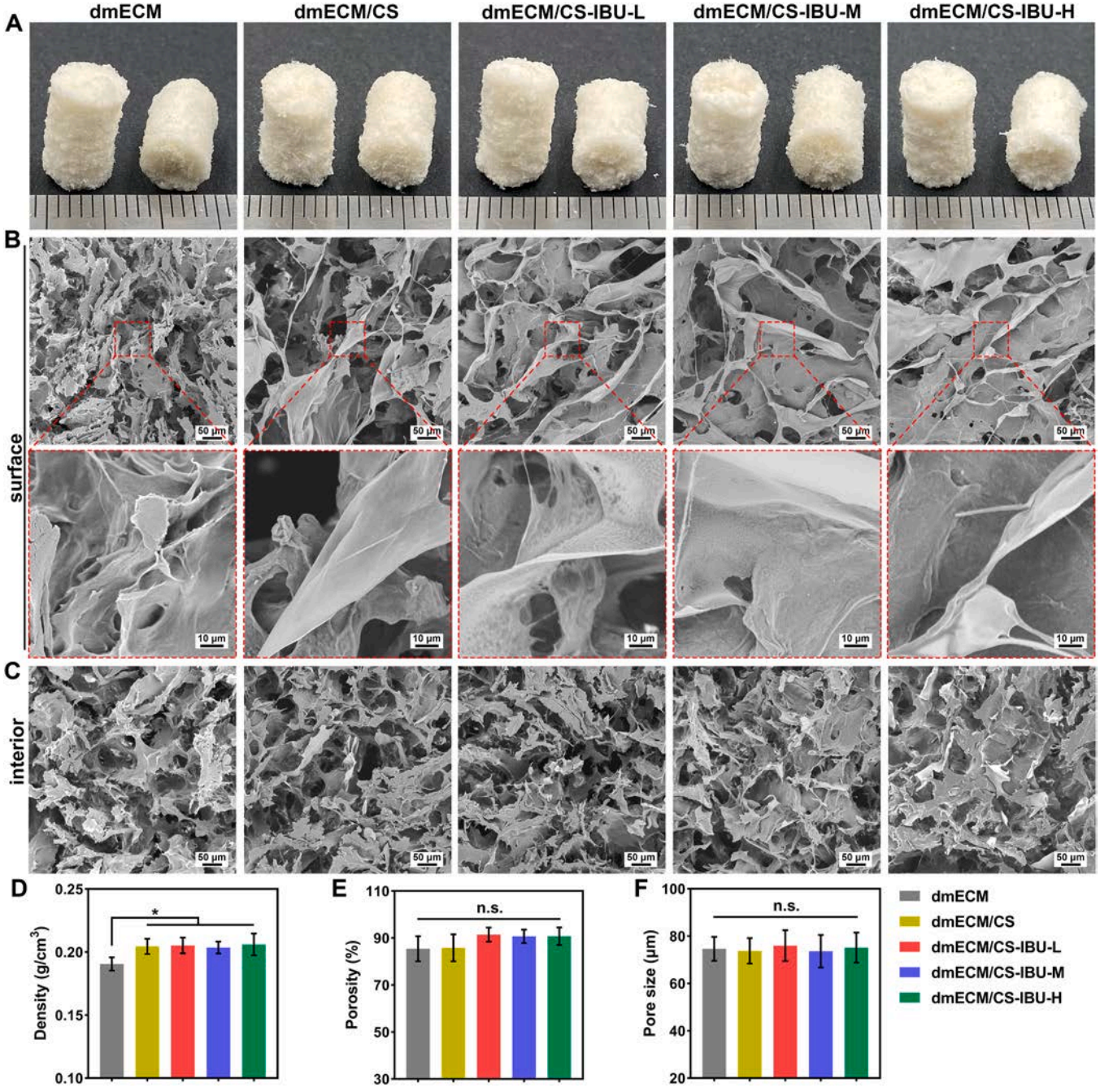

Fig. 1. Gross appearance (A) with surface (B) and internal (C) SEM images of dmECM, dmECM/CS, dmECM/CS-IBU-L, dmECM/CS-IBU-M, and dmECM/CS-IBU-H scaffolds with their densities (D), porosities (E) and pore size (F). n.s. indicates no significance, * indicates $p < 0.05$.

and the prepared powders were in uniform particles (data not shown). The dmECM had significantly fewer remaining nuclei compared to the native meniscus (Figure S1A, B), while the alcian blue staining had a similar intensity to that of the native meniscus (Figure S1C). Quantitatively, the DNA content of dmECM (5.6 ± 2.2 ng/mg) was significantly reduced compared to the native meniscus (222.9 ± 23.5 ng/mg) (Figure S1D, $p < 0.001$). The dmECM and native meniscus had comparable GAG content (Figure S1E, $p > 0.05$), with essentially no loss of GAG. The dmECM (144.9 ± 1.9 μg/mg) had a higher collagen content than the native meniscus (165.5 ± 3.8 μg/mg) (Figure S1F, $p < 0.001$). The dmECM treated by cyclic freeze-thaw grinding and DNase retained a large amount of natural components while having a high cell removal rate.

The dmECM scaffold was pre-crosslinked at 120 °C for 12 h and showed a light-yellow color in appearance. After coating with CS as well as CS-IBU, gross lamellar structures appeared on the surface of the scaffold (Fig. 1A). The surface of the scaffold introduced with CS appeared as a tightly connected lamellar structure after repeated washing with deionized water (Fig. 1B). Scattered particles appeared on the lamellar structure after the addition of IBU, probably due to the successful mixing of IBU and CS and grafting onto the surface of the scaffolds. Fine lamellar structures also appeared inside the dmECM/CS-IBU scaffold, but the introduction of CS-IBU did not change the porous structure and the small interconnected pore structure in the interior of the scaffold (Fig. 1C). The density of the scaffold increased after coating with CS-IBU (Fig. 1D, $p < 0.05$), but neither the porosity nor the pore size changed significantly (Fig. 1E, F, $p > 0.05$).

FTIR spectra of CS, IBU, and dmECM scaffolds are shown in Fig. 2A. CS showed characteristic absorption peaks at 1065 and 1027 cm^{-1}, which may correspond to the C-O stretching peaks of the secondary alcohol hydroxyl group and the primary alcohol hydroxyl group. The dmECM showed a characteristic peak at 1078 cm^{-1} corresponding to the C-O-C stretching. When the dmECM scaffold was coated with CS, a double peak at 1077 cm^{-1} to 1030 cm^{-1} was observed, confirming the successful grafting of CS. TGA was used to assess the thermal stability of dmECM and dmECM/CS-IBU scaffolds and confirm whether the products were successfully prepared. The TGA curves and derivate thermogravimetry (DTG) curves are given in Fig. 2B and C. About 2% - 10% of the weight loss occurred at the temperature below 100 ℃ in the first stage, which was due to the evaporation of water. However, it was observed that the scaffolds grafted with CS-IBU coupling lost more bound water (up to 10% of the weight loss), which could be attributed to the higher moisture absorption capacity of the coupling. The second weight loss that occurred in the range from 250 to 500 ℃ was due to the degradation of collagen (the main structural component of the ECM) [32]. XRD patterns of dmECM scaffolds are shown in Fig. 2D. Wide-angle X-ray diffraction shows sharp peaks at $2\theta = 7°$, which is the characteristic of dmECM. There is a weaker and broader peak exhibited at $2\theta = 20°$ in the diffraction pattern of dmECM/CS-IBU, indicating the presence of reduced crystallinity. This can be attributed to the successful grafting of the CS-IBU coupling and reveals that the covalent coupling leads to a significant reduction in the crystallinity of the CS-IBU

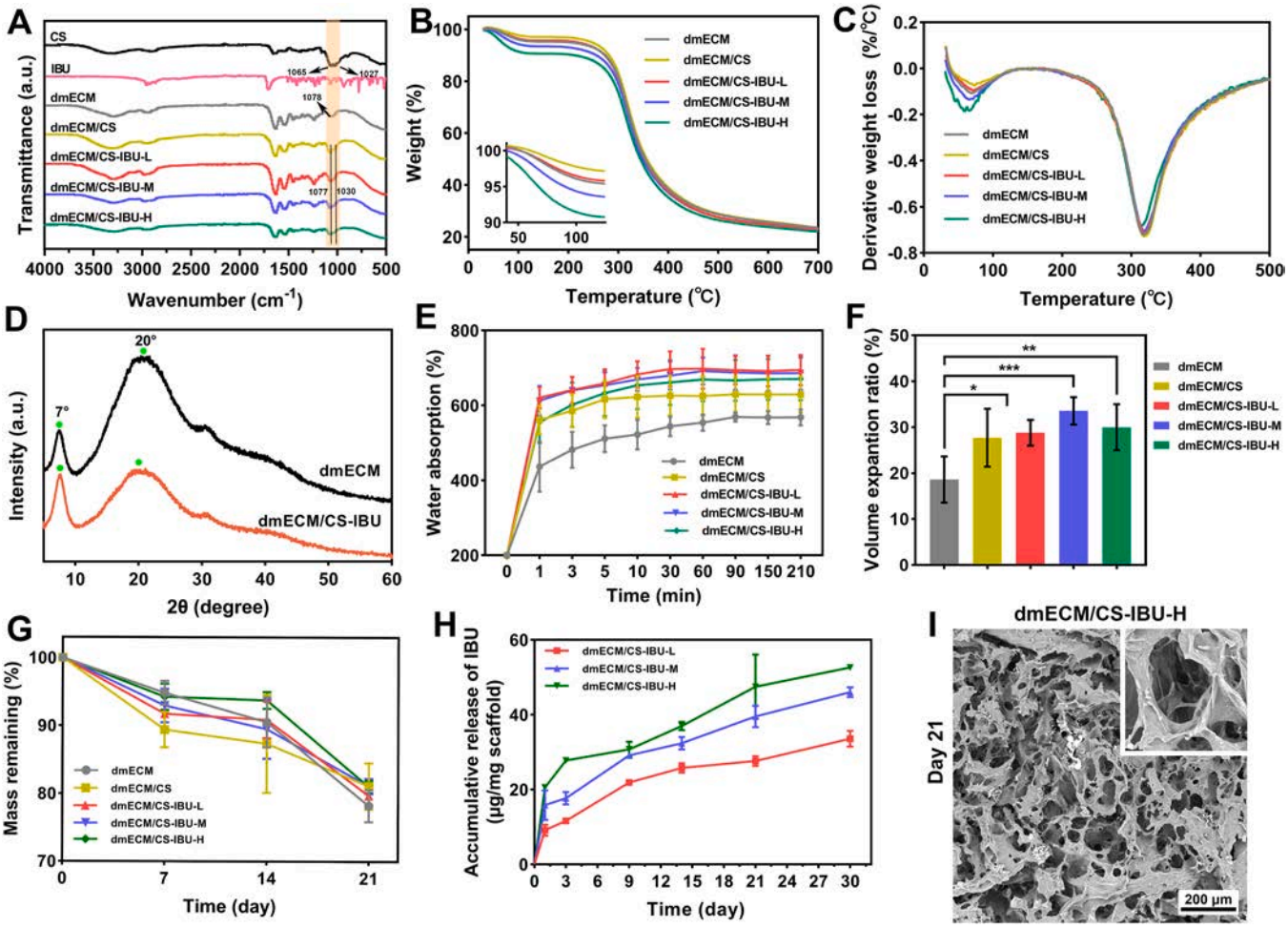

Fig. 2. FTIR (A), TGA (B) and DTG (C) curves of the scaffolds. XRD curves of dmECM and dmECM/CS-IBU (D). Water absorption curves (E) and volume expansion ratio (F) of each group of scaffolds. *In vitro* degradation curves of each group of scaffolds during 21 days (G). The *in vitro* drug release curves of dmECM/CS-IBU during 30 days (H). SEM images of dmECM/CS-IBU-H at day 21 of degradation (I). * indicates $p < 0.05$, ** indicates $p < 0.01$, *** indicates $p < 0.001$.

coupling.

The grafting of CS-IBU resulted in the dmECM scaffolds possessing stronger water absorption capacity (Fig. 2E) and greater volume expansion (Fig. 2F), which could be attributed to the presence of CS. The weight of the dmECM/CS-IBU scaffolds gradually decreased over time (Fig. 2G), and the degradation rate reached about 20% at day 21, while scaffolds maintained an intact apparent morphology as well as microstructure (Fig. 2I). As shown in Fig. 2H, the release of IBU from the dmECM/CS-IBU scaffolds showed an initial burst on the first day, but the release rate slowed down from day 3 afterward. The total amount of drug released also increased with the rise of IBU content, demonstrating the successful loading of IBU and its ability to be released slowly with scaffold degradation.

Uniaxial unconfined compression tests showed that the stress-strain curves of the dmECM/CS-IBU scaffolds (Fig. 3A) increased linearly in the first 30% strain, followed by an irregular increase in compressive strength, and then increased sharply after 60% strain until failure at 70% to 80% strain. The dmECM scaffolds had compressive strength (Fig. 3B) and compressive modulus (Fig. 3C) of 544 ± 17 kPa and 218 ± 23 kPa, respectively, and the grafting of CS and CS-IBU had no significant effect on the modulus and strength of the scaffolds ($p > 0.05$). While the dmECM scaffolds modified by CS-IBU-L as well as CS-IBU-M possessed higher damage strains compared to the raw scaffolds (Fig. 3D, 82 ± 4, 83 ± 2 *vs.* 76 ± 3%, $p < 0.05$), which may be attributed to the formation of a network structure between CS-IBU and dmECM, which enhanced the damage resistance of the dmECM scaffolds. From the compression macroscopic photographs of the scaffolds, it can be seen that the dmECM/CS-IBU scaffolds had good elasticity and maintained shape recovery when compressed up to 60% (Fig. 3E). To further verify the fatigue resistance of the scaffolds, 100 cyclic compression tests were conducted at 30% strain. Fig. 3H shows that the scaffolds had typical hysteresis loops at the initial compression, and the loading and unloading paths correspond to different trajectories. The area of the hysteresis loop of the scaffolds decreased and stabilized after the 50 (Fig. 3I) and 100 (Fig. 3J) cycles of compression. The maximum compressive stress (Fig. 3F) and compressive modulus (Fig. 3G) of the dmECM/CS-IBU scaffolds decreased as the number of cycles increased. After 100 cycles, the stress loss for all scaffolds ranged from 25–30% (Fig. 3F) and the modulus loss ranged from 27–33% (Fig. 3G). The compressive modulus of the unmodified scaffold was about 68% of the initial value after 100 cycles (Fig. 3G), whereas CS-modified and CS-IBU-M-modified scaffolds reached approximately 70%. According to our previous study [11], the dmECM scaffolds possessed good shape memory properties and elasticity, and the elasticity of the scaffolds improved even more after CS-IBU modification.

3.2. Cytocompatibility of scaffolds

NIH 3T3 fibroblasts are commonly used to evaluate the cytocompatibility of biomaterial scaffolds [33]. Live/dead cell staining showed good cytocompatibility of both dmECM and dmECM/CS-IBU scaffolds (Figure S2A). At day 1, live cells were mostly present on the dmECM scaffolds (green staining). A small number of dead cells (red dots) were found on the CS and CS-IBU modified scaffolds. At day 4, fibroblasts showed robust proliferation on all scaffolds, with a large increase in the number of cells, and the morphology was fully spread and grew along the surface of the scaffolds. Cells covered the surface of the scaffold by day 7, while the dmECM/CS-IBU-H group showed less cell

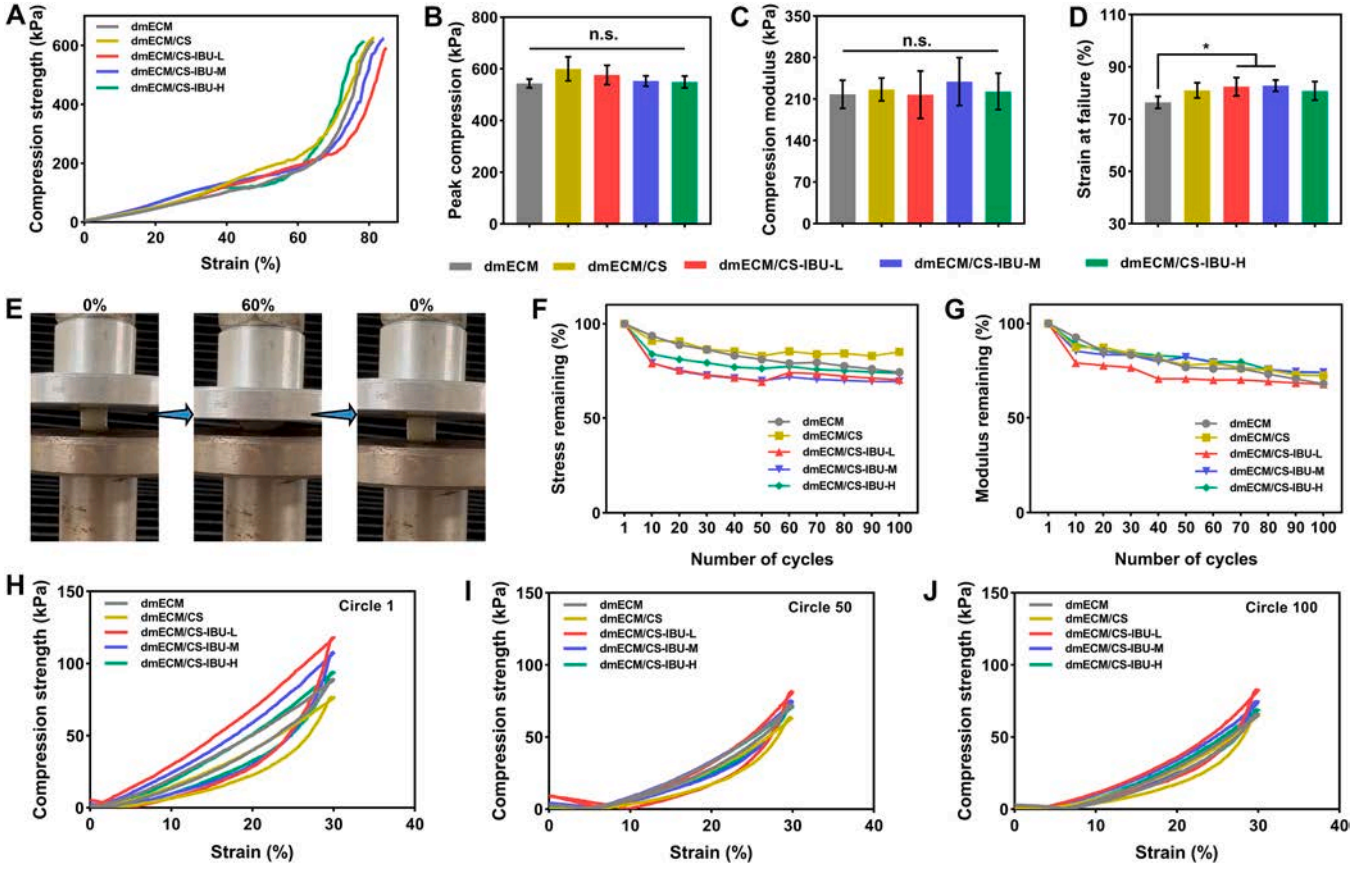

Fig. 3. Compressive stress-strain curves (A), peak compressive stress (B), compression modulus (C), and strain at failure (D) of dmECM, dmECM/CS, dmECM/CS-IBU-L, dmECM/CS-IBU-M, and dmECM/CS-IBU-H scaffolds. Photographs of the shape recovery process of the dmECM/CS-IBU scaffold in compression to 60% strain (E). The loss curves of maximum stress (F) and compressive modulus (G) of each scaffold for 100 compression cycles. The stress-strain curves of 1st (H), 50th (I), and 100th (J) cycle of each scaffold for 30% strain. n.s. indicates no significance, * indicates $p < 0.05$.

proliferation relative to the other groups. SEM images of cells showed (Figure S2B, pink) that fibroblasts were firmly adhered to the surface of the scaffolds by day 1, and the morphology was not yet fully spread, with the majority appearing as dots. At day 7 the cells proliferated and the tentacles spread out and grew along the pores of the scaffold into the interior. A decrease in the porosity of the scaffold can be observed, probably due to the adhesion of the cells onto the surface making it difficult to distinguish from the scaffold. The results of CCK-8 assay showed that fibroblasts maintained rapid growth with good viability on the scaffold up to day 7 (Figure S2C). However, the dmECM/CS group showed some inhibition of fibroblast viability compared to the dmECM group at both day 1 and day 7 ($p < 0.001$). Interestingly, the

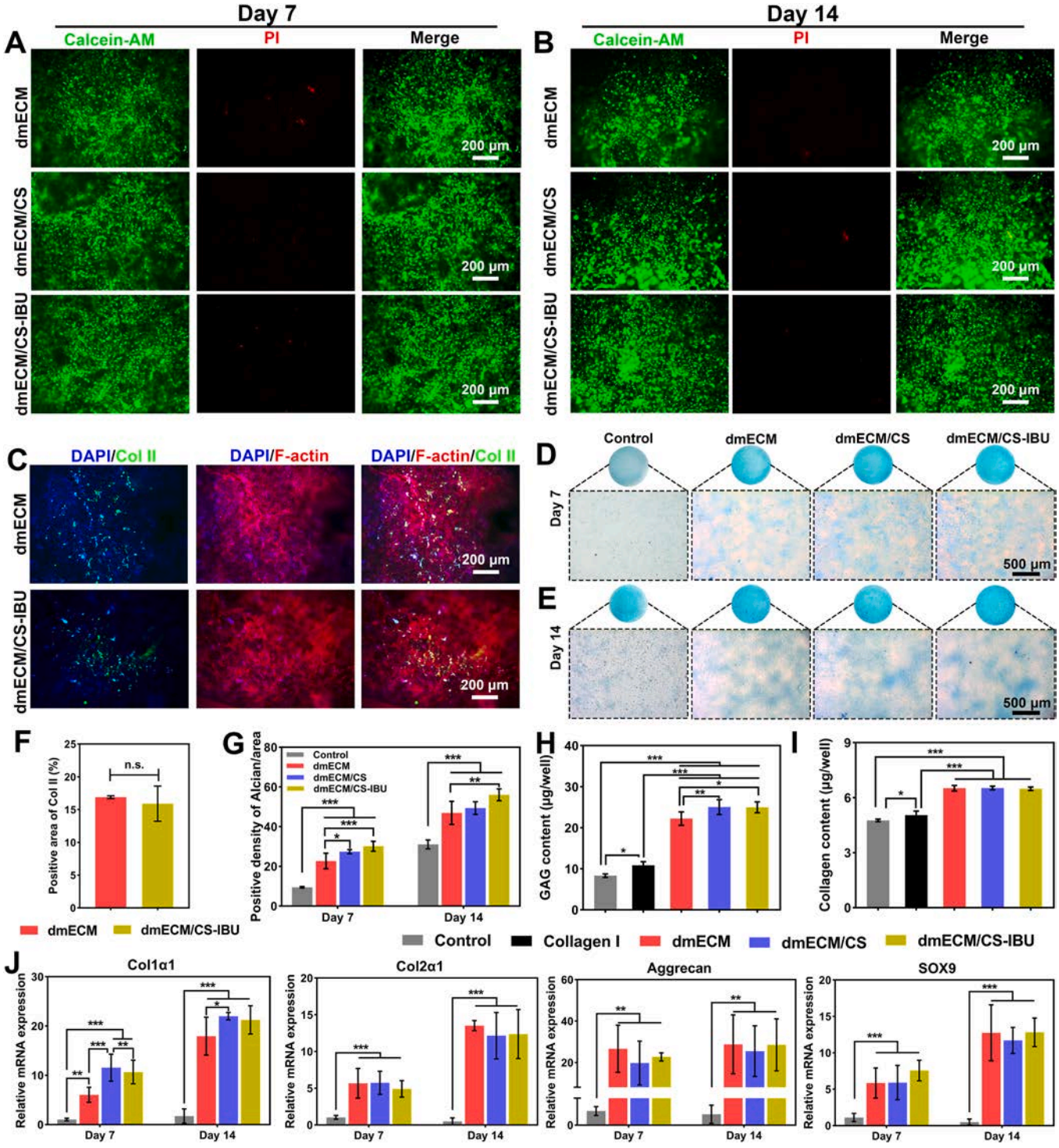

Fig. 4. Live/dead fluorescence images of articular chondrocytes on dmECM, dmECM/CS, and dmECM/CS-IBU scaffolds on days 7 (A) and 14 (B). Immunofluorescence images of chondrocytes on dmECM and dmECM/CS-IBU scaffolds on day 7 (C, blue: nucleus, red: F-actin, green: Coll-II) and the quantitative assessment of positive areas of Coll II (F). Alcian blue staining images of chondrocytes co-cultured with scaffold extracts for 7 days (D) and 14 days (E) and quantitative assessment of positive areas (G). Quantification of GAG (H) and collagen (I) levels of chondrocytes at day 7. RT-qPCR analysis results of *Col1α1, Col2α1, Aggrecan* and *SOX9* gene expression (J) of chondrocytes grown on dmECM, dmECM/CS, and dmECM/CS-IBU scaffolds. n.s. indicates no significance, * indicates $p < 0.05$, ** indicates $p < 0.01$, *** indicates $p < 0.001$.

dmECM/CS-IBU groups performed better in terms of cell viability, which was not significantly different from the dmECM group. Combined with live/dead staining and CCK-8 results, we found that higher drug loading of IBU may inhibit the proliferation of fibroblasts, but the cells remained in a high viability state.

To further investigate the effect of scaffold drug loading on cells, we co-cultured BMSCs with scaffold extract (Figure S3). Live/dead stained images showed that the morphology of BMSCs in the dmECM/CS-IBU-H group appeared atrophic with a lower number of cells at day 4, and the other groups had good cell morphology (Figure S3A). At day 7, the BMSCs were proliferating and had a typical pike or triangle morphology except for the dmECM/CS-IBU-H group (Figure S3B). The CCK-8 assay showed that the dmECM/CS-IBU-H group had an inhibitory effect on the viability of BMSCs on both day 4 and day 7 (Figure S3C, $p < 0.01$), demonstrating that higher concentrations of IBU negatively affect the proliferation and morphology of BMSCs. To meet the requirements of scaffold cytocompatibility as well as IBU drug loading, we selected the dmECM/CS-IBU-M group for further characterization (hereafter referred to as dmECM/CS-IBU).

3.3. Chondrogenesis preservation in vitro

To evaluate the effect of dmECM/CS-IBU scaffolds on the modulation of chondrocyte behavior, scaffolds were co-cultured with chondrocytes, and a series of characterizations were performed. Live/dead cell staining showed that chondrocytes grew well on dmECM, dmECM/CS, and dmECM/CS-IBU scaffolds (Fig. 4A, B). At day 7, chondrocytes grew uniformly on the surface of the scaffold pore wall, and cells were predominantly spindle-shaped (Fig. 4A). At day 14, the number of cells increased significantly and showed dense aggregated growth, while the cell morphology shifted to a rounded shape (Fig. 4B). After 7 days of culture, the morphology and behavior of chondrocytes on the scaffolds were assessed by cytoskeleton and immunofluorescence staining (Fig. 4C). Chondrocytes exhibited good cell morphology on both dmECM and dmECM/CS-IBU scaffolds, while the immunofluorescence of collagen type II was positively expressed, and quantitative statistics showed no significant difference (Fig. 4F).

The chondrocyte scratch experiment (Figure S4) showed that the wound healing rates of dmECM, dmECM/CS, and dmECM/CS-IBU at 48 hours reached up to 88 ± 1%, 92 ± 3%, and 89 ± 2%, respectively. The dmECM/CS group had the highest healing rate ($p < 0.05$), and there was no significant difference between dmECM and dmECM/CS-IBU groups, demonstrating that CS had a promoting effect on chondrocyte migration, whereas CS/IBU did not have a negative effect. The chondrocytes were co-cultured with the scaffold extract for 14 days, and the Alcian blue staining was found to be significantly deeper after 14 days of culture (Fig. 4E) compared to day 7 (Fig. 4D). Staining was darker in the scaffold groups than in the untreated group (control), and staining in the dmECM/CS-IBU group was visibly darker than in the dmECM and dmECM/CS groups. Further quantification of Alcian blue staining (Fig. 4G) revealed that the intensity of staining in the scaffold groups was much higher than that in the medium group at both 7 and 14 days ($p < 0.001$), while the intensity of staining in the scaffold after grafting CS/IBU was significantly higher than that in the dmECM group ($p < 0.01$). Furthermore, we quantified GAG (Fig. 4H) and collagen (Fig. 4I) levels in chondrocytes co-cultured for 7 days and introduced recombinant type I collagen as a positive control. Both GAG and collagen levels were increased in chondrocytes treated with type I collagen compared to the control ($p < 0.05$). In contrast, in the scaffolds-treated group, both GAG and collagen were significantly increased compared to type I collagen ($p < 0.001$). More GAG was produced in the dmECM/CS and dmECM/CS-IBU groups compared to dmECM ($p < 0.01$), and the presence of CS could possibly promote chondrocyte GAG secretion.

To further validate the induced differentiation of chondrocytes by the scaffolds, mRNA expression levels of fibrochondrocyte-related genes on the scaffolds were detected by RT-qPCR (Fig. 4J), including *Col1α1, Col2α1, SOX9* and *Aggrecan*. *Col1α1* expression in the Control group showed an up-regulation trend on day 14, while *Col2α1, SOX9*, and *Aggrecan* showed a down-regulation. In contrast, in the scaffold groups, meniscus-related genes were all increased at day 14 compared with day 7. The fibrochondrogenic gene *Col1α1* was significantly up-regulated in all scaffold groups compared to the control group ($p < 0.01$), but the expression level was higher in the dmECM/CS group than in the dmECM group ($p < 0.05$), while the expression level in the dmECM/CS-IBU group was not significantly different from that in the dmECM group. There was no significant difference in the expression of chondrocyte-related genes *Col2α1, SOX9,* and *Aggrecan* in the dmECM, dmECM/CS, and dmECM/CS-IBU groups at days 7 and 14, all of which were much higher than those in the control group ($p < 0.01$). In summary, the component of dmECM can effectively promote the meniscus-forming differentiation of chondrocytes, while the grafting of CS/IBU had no significant effect on the differentiation of chondrocytes.

3.4. Anti-inflammatory capacity of scaffolds

Many studies have shown that macrophages play an important role in the process of FBR and immune regulation [34,35]. The effect of scaffolds on RAW 264.7 macrophages was studied as shown in Fig. 5. Live-dead staining showed macrophages survived well on the scaffold and almost no dead cells were observed (red dots) (Fig. 5A). Interestingly, the presence of CS as well as IBU could be observed to promote macrophage proliferation. The dmECM scaffold had a majority of macrophages in spindle shape, in contrast, we found that dmECM/CS and dmECM/CS-IBU scaffolds could maintain the morphology of macrophages.

The anti-inflammatory ability of the scaffolds was verified by LPS-induced macrophages. The results of flow cytometry detection are shown in Fig. 5B, C. Compared with non-induced macrophages, LPS-induced macrophages were polarized toward M1 (CD86+ predominated, $p < 0.01$). When LPS-stimulated macrophages were co-cultured with scaffold extracts for 24 h, the expression of CD86 was lower and the expression of CD206 was higher in dmECM/CS-IBU scaffold compared with the dmECM and dmECM/CS scaffolds (Fig. 5C), and the corresponding fold change of M2/M1 was significantly higher (Fig. 5B, $p < 0.01$). Meanwhile, dmECM/CS-IBU scaffold-treated macrophages were not significantly different from unstimulated macrophages in terms of M2/M1 ratio (Fig. 5B, $p > 0.05$). These results indicated that the introduction of IBU can effectively reduce the M1 phenotype of macrophages and increase the M2 phenotype, and the composite scaffolds had good anti-inflammatory capacity.

To further verify the anti-inflammatory effects of the composite scaffolds, the expression of pro-inflammatory genes *IL-6, IL-1β,* and anti-inflammatory gene *IL-10* in LPS-induced macrophages were investigated after 24 h of treatment with different scaffold extracts (Fig. 5D). The results showed that the scaffolds modified with CS and IBU significantly down-regulated the expression levels of *IL-6* and *IL-1β* ($p < 0.01$), while dmECM/CS-IBU obtained lower expression of pro-inflammatory genes. Notably, although dmECM/CS did not trigger high expression of anti-inflammatory genes, the addition of IBU greatly upregulated *IL-10* expression ($p < 0.01$).

The anti-oxidative effect of the scaffold on LPS-induced macrophages was examined using DCFH-DA as a ROS probe (Fig. 5E, F). It can be observed that the ROS fluorescence positivity was much higher in control and dmECM groups than in dmECM/CS and dmECM/CS-IBU groups (Fig. 5E, green). Quantitative statistics (Fig. 5F) of the fluorescence images showed that the ROS levels were high in the control group and dmECM, while dmECM/CS and dmECM/CS-IBU significantly lower ROS levels ($p < 0.001$), with dmECM/CS-IBU reaching the lowest ROS level of 1.99%. CS and IBU have powerful free radical scavenging ability on M1 macrophages. LPS-induced macrophages produced more NO ($p < 0.001$), whereas CS and IBU significantly inhibited NO production (Fig. 5G, $p < 0.05$). Therefore, the dmECM/CS-IBU scaffold significantly

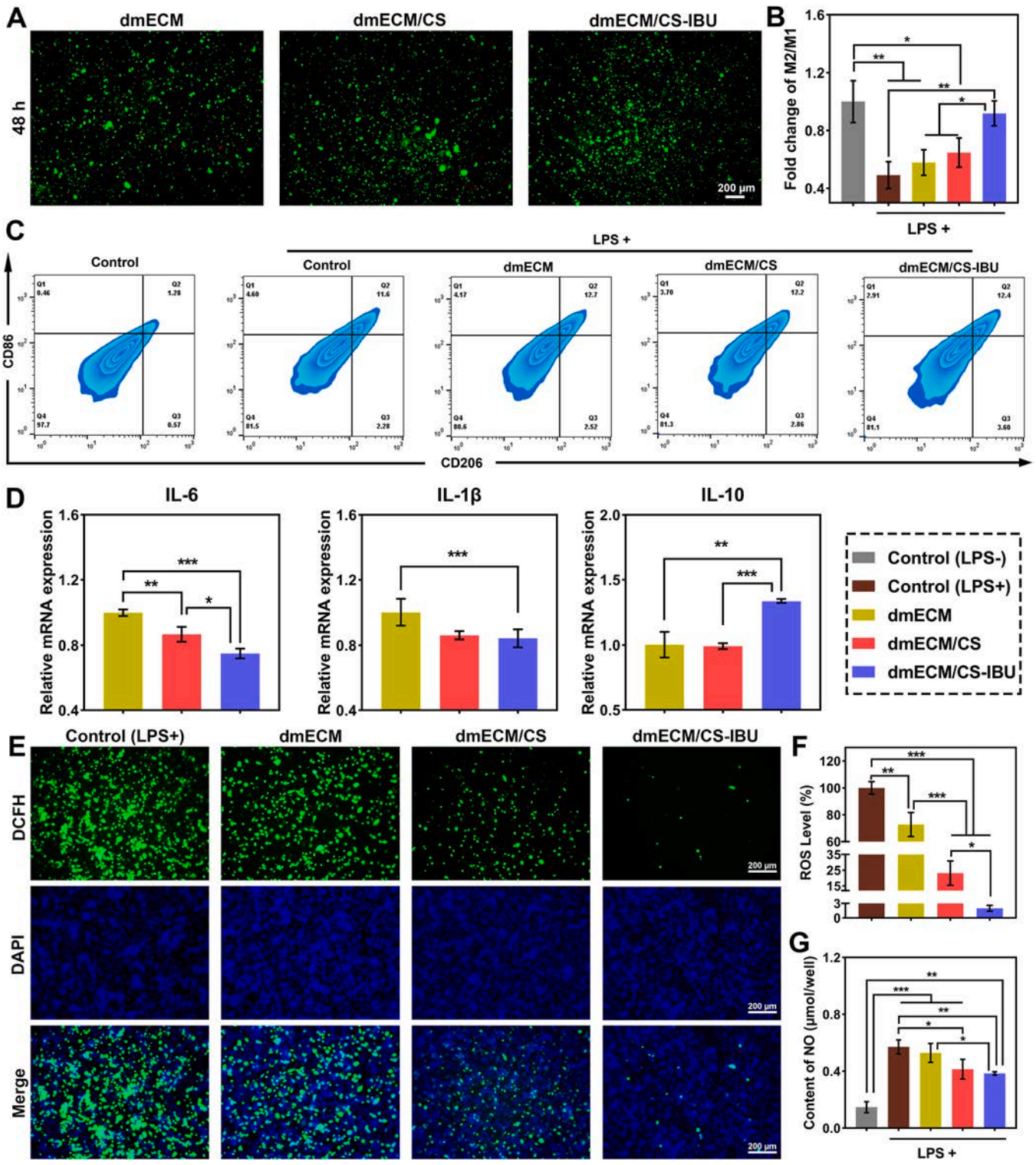

Fig. 5. Live/dead fluorescence images of RAW264.7 on dmECM, dmECM/CS, and dmECM/CS-IBU scaffolds for 48 hours (A). Flow cytometry detection of macrophage M2 type marker CD206 as well as M1 type marker CD86 expression levels (C) and fold change quantification (B). RT-qPCR analysis of the expression levels of M1 type-related genes *IL-6, IL-1β*, and M2 type-related genes *IL-10* (D). Fluorescence images of oxidized levels of RAW264.7 macrophages after 24 h of treatment with scaffold extracts (E, blue: nuclei, green: DCFH-DA) and quantitative fluorescence statistics (F). NO level of RAW264.7 macrophages (G). * indicates $p < 0.05$, ** indicates $p < 0.01$, *** indicates $p < 0.001$.

attenuates inflammation and has strong anti-inflammatory activity.

H&E staining (Figure S5A) shows that cells infiltrated all scaffolds after 7 days, with the scaffolds being more loosely packed in the dmECM group, and the scaffold morphology being denser in the dmECM/CS and dmECM/CS-IBU groups. Masson trichrome staining (Figure S5B) showed moderate collagen deposition in the pores of the scaffolds on day 7, with significantly more collagen deposition in the dmECM/CS and dmECM/CS-IBU scaffolds than in the dmECM scaffolds. The acute inflammatory response of scaffolds after 7 day subcutaneous implantation was analyzed by immunohistochemical staining for CD11b+

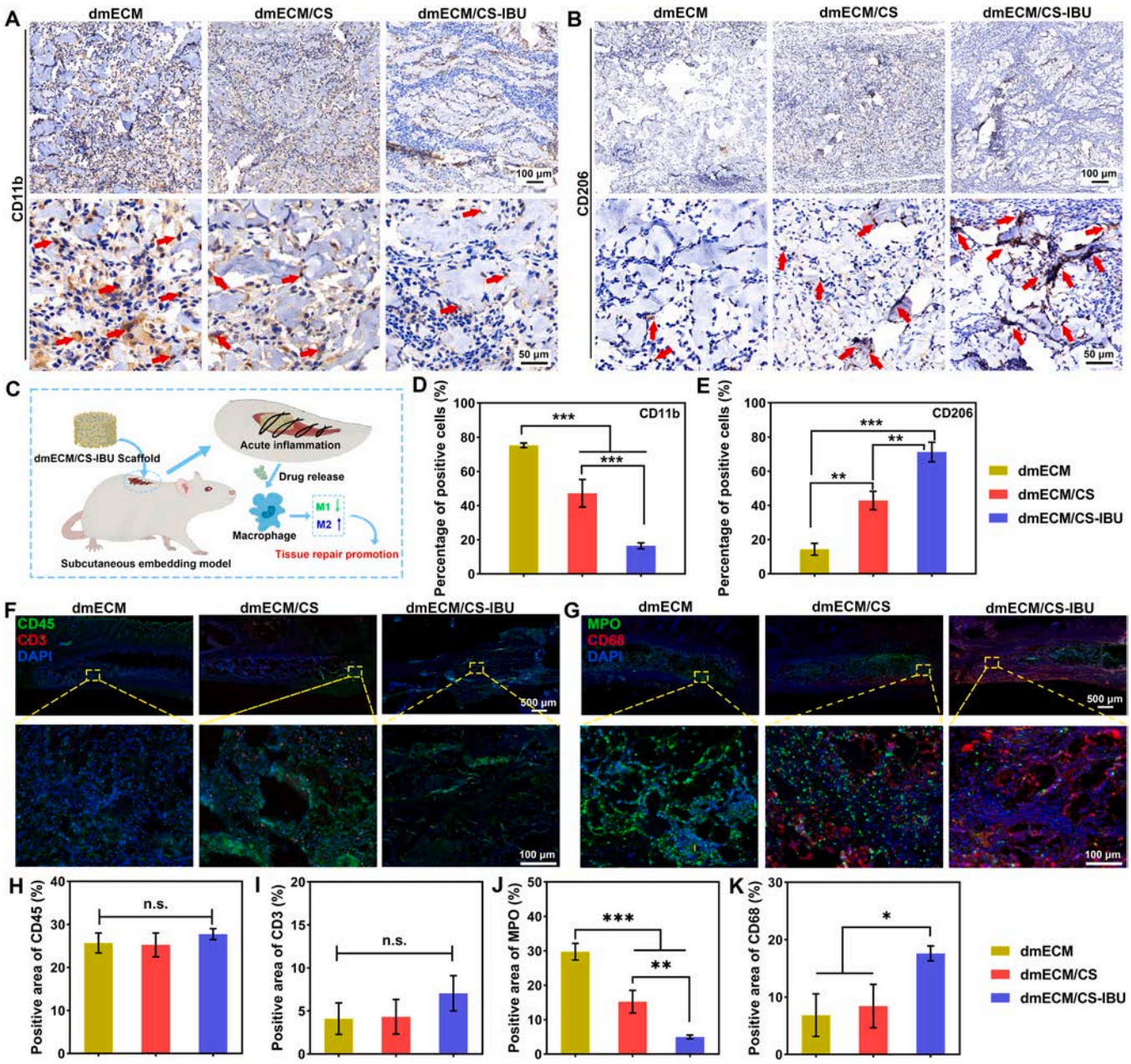

Fig. 6. Immunohistochemical staining results after 7 days of subcutaneous embedding of dmECM, dmECM/CS, and dmECM/CS-IBU scaffolds in a rat model. Immunohistochemical images of the M1-type macrophage marker CD11b (A) and the M2-type macrophage marker CD206 (B). Illustration of the relief of acute inflammation by dmECM/CS-IBU scaffold (C). Quantitative results of the percentage of CD11b (D) and CD206 (E) positive cells. Immunofluorescent staining of leukocyte (CD45+) and T-cell (CD3+) at day 7 (F). Immunofluorescent staining of neutrophil (MPO+) and macrophage (CD68+) at day 7 (G). Quantitative results of positive area of CD45 (H), CD3 (I), MPO (J) and CD68 (K). * indicates $p < 0.05$, ** indicates $p < 0.01$, *** indicates $p < 0.001$.

(Fig. 6A) and CD206+ (Fig. 6B). The dmECM scaffolds showed a higher acute inflammatory response, whereas dmECM/CS had a decrease in proinflammatory macrophages (M1, CD11b +, red arrows), with CD11b+ macrophages mainly concentrated within the pores of the scaffolds or on the surface of the matrix. In the dmECM/CS-IBU scaffolds, on the other hand, there were few M1 macrophages found only on the surface of matrix particles. It was seen from the quantitative result of CD11b+ cells (Fig. 6D) that the percentage of positive cells in dmECM/CS-IBU (16 ± 2%) was much lower than that in the dmECM group (75 ± 1%, $p < 0.001$) and the dmECM/CS group (47 ± 8%, $p < 0.001$). Correspondingly, the highest number of anti-inflammatory-type macrophages (M2, CD206+) was observed in the dmECM/CS-IBU scaffolds, whereas few definitive CD206+ cells were seen in the dmECM and dmECM/CS groups (red arrows). Further quantitative analysis (Fig. 6E) showed that the percentage of CD206+ macrophage positivity was significantly higher in the dmECM/CS-IBU group (71 ± 6%) than in the dmECM group (14 ± 3%, $p < 0.001$) and dmECM/CS (43 ± 5%, $p < 0.01$). To further analyze the immune cell subsets, immunofluorescence staining for the leukocyte (CD45+), T-cell (CD3+), neutrophil (MPO+), and macrophage (CD68+) was analyzed (Fig. 6F, G). There was no significant difference in CD45+ and CD3+ between the different groups (Fig. 6F, H, I). A large number of neutrophil (MPO+) was found in the dmECM group (Fig. 6G), and the positivity of MPO was significantly reduced in the dmECM/CS and dmECM/CS-IBU groups (Fig. 6J, $p < 0.01$). Neutrophils were found only in the central region of the dmECM/CS-IBU scaffold, and a large number of pan-macrophages (CD68+) appeared around the edge region of the scaffold (Fig. 6G). The positivity of CD68 was significantly lower in the dmECM group and the dmECM/

CS group than in the dmECM/CS-IBU group (Fig. 6K), suggesting that the presence of CS-IBU could promote tissue repair. The dmECM/CS-IBU scaffold rapidly attenuated the acute host response and induced macrophage M2-type polarization during the initial phase of subcutaneous implantation, accelerating the process of tissue repair and regeneration.

3.5. In situ evaluation

The meniscus cylindrical defect model was constructed to further validate the ability of the dmECM/CS-IBU scaffold to repair meniscus defects (Fig. 7A). After 3 months, there was no obvious regenerated tissue at the defect site in the control group, while the regeneration of the dmECM/CS-IBU group was significantly better than that of the dmECM (Fig. 7B). H&E staining shows (Fig. 7C) that there was almost no regenerated tissue at the defect interface in the control group, indicating low spontaneous regeneration of the meniscus. In the group of dmECM, the repair interface was filled with more neoplastic tissue, but the tissue integration was inadequate, and the neoplastic tissue in the dmECM/CS-IBU was more adequately integrated with the surrounding tissue. Many ovoid chondrocyte-like cells could be observed in the dmECM/CS -IBU (Fig. 7C, yellow arrows), with uneven spacing of luminal spaces, which exhibited mature cartilage luminal structures similar to that of the native meniscus, while only a small number of cartilage-like cells were observed in dmECM.

Toluidine blue staining was performed on the tissues (Fig. 7D), and the defects were negative for toluidine blue staining in the control group. The repair interface could be observed in dmECM, and the defect repair area showed a strong pass-through positive toluidine blue staining. In dmECM/CS-IBU, the repair interface could not be observed, but it also showed a strong positive toluidine blue staining, similar to the surrounding tissue, indicating the good integration of neoplastic tissue with the surrounding normal tissue. In the safranin O staining (Fig. 7E), almost no safranin O positivity was observed in the control group. Although chondrocyte-like cells could be observed in dmECM, only a small amount of ECM was stained by safranin O. In contrast, in the dmECM/CS-IBU, almost the entire ECM of the white zone was positive for safranin O.

To further evaluate the repair of meniscus defects, the tissues were stained with type I collagen (Fig. 7F) and type II collagen (Fig. 7G). In the control group, both type I collagen and type II collagen staining were negative at the defect interface because of the absence of regeneration. Positive pericellular staining was evident in type I and type II collagen staining of the native meniscus. The dmECM group showed weakly positive type I collagen staining and type II collagen staining. Type I collagen staining (Fig. 7F) was positive and highly expressed in the same way in the dmECM/CS-IBU and native meniscus. In the native meniscus, type II collagen staining was mainly concentrated at the edges of the white zone, while the repaired areas in the dmECM/CS-IBU showed large areas of strong positive type II collagen staining (Fig. 7G).

Histologic evaluation with H&E staining and toluidine blue staining was used to detect cartilage degeneration in the femoral condyle (FC, Fig. 8A) and tibial plateau (TP, Fig. 8B) in each group. The histologic results were consistent with the macroscopic results. After 12 weeks, cartilage discontinuities on the surface of the FC and TP were observed in the Control group, with marked progression of degeneration (red arrows), and the formation of vertical fissures could be seen. The dmECM had irregular defects on the surface of the cartilage but the overall condition was significantly better than that of the control group. Tibial cartilage (Fig. 8B) had reduced chondrocytes with distinct areas of clonal chondrocytes (red dashed box). In contrast, the mildest cartilage degeneration was observed in the dmECM/CS-IBU, presenting a smooth and continuous surface with no effect on the nuclear matrix of the subchondral cells. Based on the International Cartilage Repair Society (ICRS) score (Fig. 8C, D), the control group had the most severe cartilage damage, while the dmECM/CS-IBU showed the best cartilage protection.

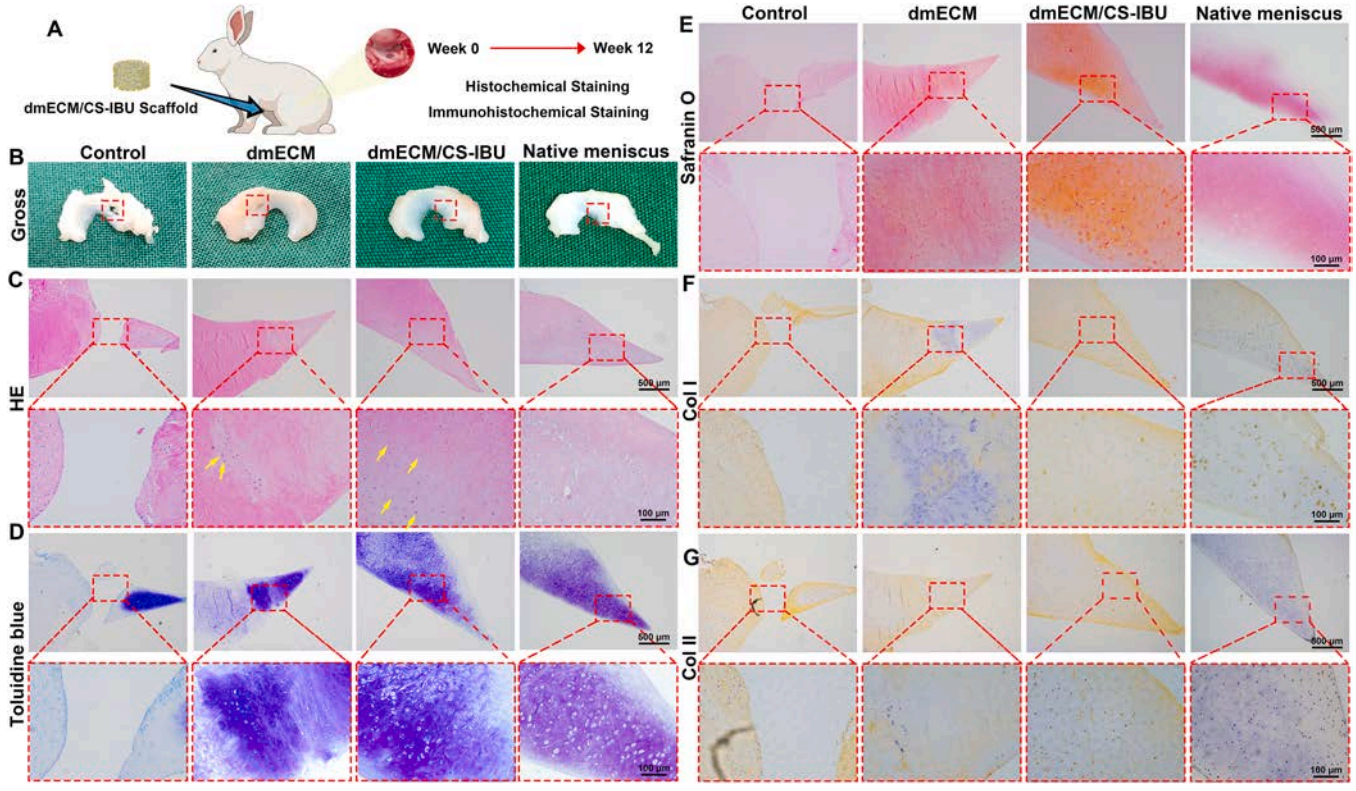

Fig. 7. Schematic illustration of the process of scaffolds implantation in white zone defects of the meniscus in rabbits (A). Macroscopic images of the meniscus acquired 12 weeks after surgery (B). H&E staining of cross-sections of regenerated meniscus tissue after 12 weeks (C). Toluidine blue staining (D) and Safranin-O staining (E) of a cross section of meniscus tissue. Type I collagen staining (F) and type II collagen staining (G) of cross-sections of regenerated meniscus tissue.

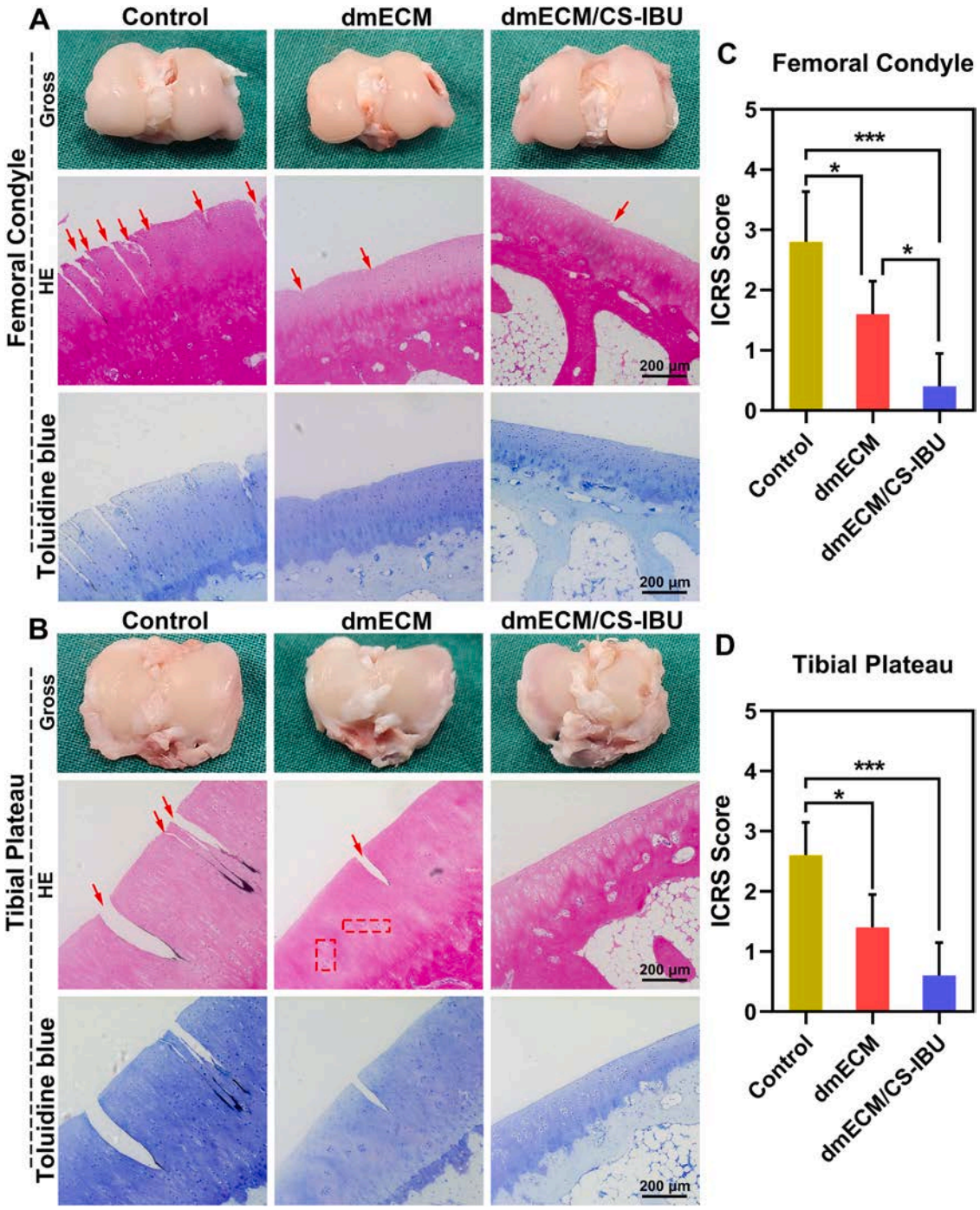

Fig. 8. Macroscopic images, H&E staining and toluidine blue staining of the femoral condyles (A) and the tibial plateaus (B) 12 weeks after surgery (Red arrows: Cartilage degradation site. Red boxes: zones of cloning chondrocytes). International Cartilage Repair Society (ICRS) scores of articular cartilage surfaces in the femoral condyle (C) and tibial plateau (D). * indicates $p < 0.05$, *** indicates $p < 0.001$.

Thus, the dmECM/CS-IBU scaffold significantly reduced cartilage wear due to meniscal injury.

4. Discussion

Tissue engineering scaffolds should have appropriate mechanical strength as well as suitable pore structure to provide physical support as well as an integrated matrix for tissue repair and regeneration [36,37]. The meniscus has a special physiological structure with dense ECM, while the vulnerable white zone has almost no blood vessels and nerves, which probably inhibits cellular infiltration and greatly limits tissue regeneration. Therefore, the development of tissue-engineered scaffolds with a three-dimensional porous structure is crucial for endogenous cellular infiltration of dense tissues and *in situ* regeneration of functional tissues [36]. Previously, we reported a meniscus decellularization method by cyclic freeze-thaw milling combined with DNase and successfully prepared elastic and porous dmECM scaffolds [11]. We found that the dmECM scaffold retained many meniscus-specific bioactive components and could maintain the chondrogenic differentiation of chondrocytes while preserving good mechanical strength and elasticity. The meniscus includes fibroblast-like cells, chondrocytes, and fibrochondrocytes, of which chondrocytes are located in the superficial zone

and synthesize large amounts of type II collagen and sGAG, which play an important role in meniscus healing [38]. Meanwhile, sGAG and collagen fibers are crucial in the maintenance of mechanical properties [39] and provide an appropriate microenvironment during the repair process [38]. Therefore, the retention of bioactive components such as sGAG and collagen is very important in the application of scaffolds [40]. The dmECM scaffolds had good elasticity and provided a favorable growth environment for chondrocytes, which may be attributed to the mild decellularization method retaining a large number of bioactive components (Figure S1). However, the scaffolds were not stable enough to be damaged upon multiple compression and also caused severe inflammation in the body. In this study, we carried out some optimization. The porous structure of the dmECM scaffolds was formed by physical extrusion molding in a mold (Fig. 1). The appropriate pore structure resulted in good cytocompatibility of the scaffold, which supported cell adhesion as well as growth entry and proliferation (Figs. 4 and S2). The scaffolds support cell migration for better tissue repair *in vivo*.

It is crucial to mimic the microstructure and mechanical properties of natural tissues to achieve rapid tissue regeneration and to protect cells that are under strain during physical activity [41]. The meniscus is located between the femoral condyle and the tibial plateau and plays a key role in maintaining joint stability, absorbing shock, and cushioning impact. Because the meniscus is subjected to high pressure during daily activities, mechanical match between the implanted graft and meniscus tissue is a prerequisite for successful graft-tissue integration. Mechanical mismatch is likely to destroy the implant, inferior integration, and abrasive damage to the cartilage interface. Through increasing the degree of cross-linking, it is hoped that the structure of the scaffold will be more stable. We first physically pre-crosslinked them by dehydrothermal treatment and then chemically crosslinked and functionalized scaffolds by EDC/NHS. A portion of IBU was grafted onto CS via amide bond to form CS-IBU, and CS-IBU as well as unreacted CS and IBU coexisted in the system. During the functionalization process, the dmECM scaffolds underwent self-crosslinking via EDC/NHS on the one hand, and CS-IBU and independent CS, IBU were grafted onto dmECM via amide bonds on the other hand. The high density as well as the high degree of cross-linking endowed the dmECM/CS-IBU scaffolds with a stable structure, mechanical strength matching that of natural tissues, and high elasticity (Fig. 3). After 100 cycles, the dmECM/CS-IBU scaffold experienced less stress as well as loss of modulus, while being able to regain its shape after 60% compression. The superior mechanics make the dmECM/CS-IBU scaffold less susceptible to disruption after implantation and can deform synergistically with natural meniscal tissue, which is more conducive to the repair of meniscal injuries.

Chitosan is commonly used in cartilage tissue engineering studies [42,43]. Chitosan of appropriate molecular weight promotes chondrocyte proliferation [44], and contributes to cell/matrix interactions. Given the GAG-like structure, chitosan has significant advantages in stimulating chondrogenesis [45]. NSAIDs are widely used as symptomatic therapeutic agents in osteoarthritis, but their effects on cartilage remain controversial. It has been shown that IBU has no side effects on chondrocytes under normal conditions and can transform the chondrocyte transcriptome into an anti-inflammatory phenotype in an inflammatory environment [46]. Allogeneic articular chondrocytes (AC) are a suitable cell source to compensate for the shortage and limitations of autologous white zone meniscal cells [47]. In this study, we verified the effect of dmECM/CS-IBU scaffolds on chondrocyte phenotype. Aggregate expression of type II collagen and up-regulation of the expression levels of cartilage-related genes (*Col2α1, aggrecan,* and *SOX9*) was observed on chondrocytes cultured on dmECM/CS-IBU scaffolds (Fig. 4), proving that scaffolds could effectively regulate the function of chondrocytes. Interestingly, the dmECM/CS-IBU group showed some promotional up-regulation in the expression level of the fibrocartilage-related gene (*Col1α1*), suggesting that grafting of CS/IBU could synergistically enhance the induction of fibrocartilage cells by dmECM to some extent. Due to the specificity of avascularity, the ability of cell recruitment is important for the white zone meniscus repair process. In the scratch healing experiment (Figure S4), scaffolds were found to promote chondrocyte migration. In summary, we demonstrated that the dmECM/CS-IBU scaffolds could recruit and promote chondrocyte proliferation. Meanwhile, scaffolds promote the fibrochondrogenic differentiation of chondrocytes and maintain the high expression of type II collagen while promoting the expression of type I collagen.

Previously, we found that although the dmECM scaffold retained meniscus tissue-specific activity but it caused acute inflammatory response when implanted *in vivo* [11]. In knee-related surgeries, FBR of implants often brings complications such as joint pain, effusion, and swelling, while adverse effects such as reduced joint mobility may even require reoperation [48]. Therefore, it is crucial to find a suitable solution or mitigation of acute inflammation based on a biologically active dmECM scaffold. Our group has developed a series of biomaterials combining small-molecule anti-inflammatory drugs with polymeric materials, which have been successfully used to prevent tendon adhesion [49] and promote abdominal wall defects [26]. Inspired by the results, in this study, we found that a free carboxyl group on the small molecule drug IBU can react with the amino group on the polymeric material CS as well as dmECM to confer a certain degree of anti-inflammatory and antioxidant capacity to dmECM. The surface of the dmECM/CS-IBU scaffold was grafted with more CS-IBU, while a small amount of film was also present inside the scaffold (Fig. 1). In the initial stage of scaffold implantation in the body, the externally wrapped film would be the first to come off and contribute to the rapid reduction of acute inflammation during the pre-implantation phase. Over time, the scaffold slowly degraded and the internal CS-IBU was gradually released, which can play a role in continuously regulating the balance of inflammation *in vivo*, laying the foundation for the subsequent repair phase.

ROS is a biochemical weapon for immune cells to fight against infecting bacteria, while oxidative stress (OS) is a state of imbalance between oxidative and antioxidant effects in the body. Excess oxides including ROS and reactive nitrogen species (RNS) affect knee joint homeostasis [50], so inhibition of the OS signaling pathway is critical for creating a favorable microenvironment for meniscus repair. The dmECM/CS-IBU scaffold showed effective anti-inflammatory and antioxidant action against macrophage RAW 264.7 while maintaining cytocompatibility (Fig. 5). In dmECM/CS-IBU-treated macrophages, reductions in oxidized ROS and NO levels were observed (Fig. 5E-G), suggesting that the scaffolds were effective in scavenging free radicals and protecting the meniscus from inflammations during repair. Subcutaneous embedding experiments similarly demonstrated that dmECM/CS-IBU effectively cleared M1 macrophages and accelerated M2-type polarization of macrophages in the first 7 days (Fig. 6). Neutrophils are the most abundant circulating leukocytes in humans and the first immune cells recruited at sites of inflammation [51]. Grafting of IBU significantly reduced neutrophils and presented an increase in M2-type macrophages starting from the outside of the scaffold (Fig. 6). Thus, the dmECM/CS-IBU scaffold can effectively respond to acute inflammation, modulate the cascade transition to an anti-inflammatory environment, and lay the foundation for further meniscal injury repair.

To further evaluate the repair effect of the dmECM/CS-IBU scaffolds, we constructed an *in-situ* repair model in rabbits (Figs. 7 and 8). The results of the *in vivo* experiments over 3 months showed that the dmECM/CS-IBU scaffold was very effective in the repair of the white zone of the meniscus. It can be observed in the tissue sections (Fig. 7) that the dmECM group was in the process of the repair period and the interface of the defect was obvious. In contrast, the dmECM/CS-IBU scaffold showed a significant improvement in the speed of repair, with the defect well integrated with the surrounding tissues, and the presence of a large number of mature chondrocyte-like cells and cartilage traps, and the histological features largely resembling those of the native meniscus. The repair capacity of the dmECM group was already

impressive given the strong cartilage-inducing ability of the dmECM active ingredient, and the addition of the anti-inflammatory ingredient CS and IBU allowed the scaffolds to gain full integration at the site of the meniscal defect at 12 weeks. The biological process of FBR induced by most biomaterials consists of four phases: protein adsorption, acute inflammation, chronic inflammation, and fibrosis [52]. The dmECM/CS-IBU scaffold was effective in attenuating the acute inflammatory process in the early stage of repair (Fig. 6E), accelerating the initial macrophage M2 polarization, and effectively terminating the continued progression of FBR to chronic inflammation. During *in vivo* repair, the inflammation-modulating effect of the dmECM/CS-IBU scaffold led to a smoother meniscal healing process. Previous studies have shown that type I collagen is present in most areas of the meniscus, whereas type II collagen is concentrated in the white areas [53]. Stabilized type I collagen has an equally important role in the meniscus [54]. The dmECM/CS-IBU scaffold upregulated not only type II collagen expression in chondrocytes but also type I collagen expression *in vitro* and *in situ* (Figs. 4 and 7). Meanwhile, the dmECM/CS-IBU scaffold demonstrated protection of the cartilage of the femoral condyle and tibial plateau (Fig. 8). These biological results confirm the great potential of the dmECM/CS-IBU scaffold in the repair of the white zone meniscus, which has high bioactivity as well as suitable anti-inflammatory capacity for *in situ* regeneration and remodeling of meniscal white zone defects.

There are some limitations in this study. Reconstructed decellularized extracellular matrix scaffolds are limited in shape, and meniscal white zone injuries are usually irregular, limiting clinical scenarios, and we need to explore more decellularized extracellular matrix forms such as hydrogels. It is difficult for current regenerative scaffolds to mimic the unique ECM structure of the meniscus, and it may be possible to mimic the anisotropic microstructure by dmECM and synthetic polymers using 3D printing. In addition, we did not have a clear assessment of the anti-inflammatory mechanism and repair process of the scaffolds *in situ*, and more adequate studies are needed in the future.

5. Conclusion

We demonstrate a safe, convenient, and scalable method through the mutual reaction between dmECM, CS, and IBU, complemented by dual cross-linking to prepare elastic and anti-inflammatory decellularized scaffolds that can induce meniscus tissue regeneration. The scaffolds have proper strength and elasticity, as well as good porosity to support cell growth and tissue integration. The scaffold showed good anti-inflammatory and antioxidant properties, while promoting the repair of chondrocytes as well as meniscus damage *in vitro* and *in vivo*. Overall, we demonstrated the important role of inflammatory modulation in meniscus repair and successfully integrated dmECM and anti-inflammatory components, showing rapid tissue integration in meniscus tissue defects. The inflammation-modulating meniscus scaffolds have potential applications in promoting injury repair in the white zone of the meniscus and can be an effective alternative to conventional meniscus repair.

CRediT authorship contribution statement

Yangfan Ding: Writing – original draft, Methodology, Investigation, Data curation, Conceptualization. **Moran Huang:** Methodology, Investigation, Data curation. **Pengfei Cai:** Investigation, Data curation. **Xiao Yu:** Validation. **Jie Cui:** Methodology. **Binbin Sun:** Methodology. **Xiumei Mo:** Supervision. **Changrui Lu:** Writing – review & editing, Supervision. **Jiwu Chen:** Writing – review & editing, Supervision, Funding acquisition. **Jinglei Wu:** Writing – review & editing, Validation, Supervision, Methodology, Investigation, Funding acquisition, Conceptualization.

Declaration of competing interest

The authors declare that they have no known competing financial interests or personal relationships that could have appeared to influence the work reported in this paper.

Acknowledgments

This study is supported by the Fundamental Research Funds for the Central Universities (2232023D-09 and CUSF-DH-T-2023025). This work was financially supported by the National Natural Science Foundation of China (31900949, 82372491, and 82172509).

Supplementary materials

Supplementary material associated with this article can be found, in the online version, at doi:10.1016/j.actbio.2025.02.043.

References

[1] H. Roos, M. Laurn, T. Adalberth, E.M. Roos, K. Jonsson, L.S. Lohmander, Knee osteoarthritis after meniscectomy: Prevalence of radiographic changes after twenty-one years, compared with matched controls, Arthritis Rheum. 41 (4) (1998) 687–693.
[2] Z. Abpeikar, M. Javdani, S.A. Mirzaei, A. Alizadeh, L. Moradi, M. Soleimannejad, S. Bonakdar, S. Asadpour, Macroporous scaffold surface modified with biological macromolecules and piroxicam-loaded gelatin nanofibers toward meniscus cartilage repair, Int. J. Biol. Macromol. 183 (2021) 1327–1345.
[3] C. Scotti, M.T. Hirschmann, P. Antinolfi, I. Martin, G.M. Peretti, Meniscus repair and regeneration: review on current methods and research potential, Eur. Cell Mater. 26 (2013) 150–170.
[4] L. Schenk, L. Bethge, A. Hirschmann, R. Berbig, U. Lüthi, M.P. Arnold, M. T. Hirschmann, Ongoing MRI remodeling 3–7 years after collagen meniscus implantation in stable knees, Knee Surg. Sports Traumatol. Arthrosc. 28 (4) (2019) 1099–1104.
[5] G.A. Lucidi, P. Agostinone, S. Di Paolo, A. Grassi, A. Pierangeli, G. Dal Fabbro, S. Zaffagnini, Loss of chondroprotection of medial collagen meniscus implant (CMI) at 20-year follow-up, J ISAKOS. 9 (2) (2024) 116–121.
[6] S.F. Badylak, Xenogeneic extracellular matrix as a scaffold for tissue reconstruction, Transpl. Immunol. 12 (3–4) (2004) 367–377.
[7] F.A. Monibi, J.L. Cook, Tissue-Derived Extracellular Matrix Bioscaffolds: Emerging Applications in Cartilage and Meniscus Repair, Tissue Eng. Part B Rev. 23 (4) (2017) 386–398.
[8] J. Wu, Q. Ding, A. Dutta, Y. Wang, Y.H. Huang, H. Weng, L. Tang, Y. Hong, An injectable extracellular matrix derived hydrogel for meniscus repair and regeneration, Acta Biomater. 16 (2015) 49–59.
[9] X. Wang, J. Zhu, B. Sun, Q. Jin, H. Li, C. Xia, H. Wang, X. Mo, J. Wu, Harnessing electrospun nanofibers to recapitulate hierarchical fibrous structures of meniscus, J. Biomed. Mater. Res. B Appl. Biomater. 109 (2) (2021) 201–213.
[10] H. Li, X. Wang, J. Liu, Z. Liu, H. Wang, X. Mo, J. Wu, Nanofiber configuration affects biological performance of decellularized meniscus extracellular matrix incorporated electrospun scaffolds, Biomed. Mater. 16 (6) (2021) 065013.
[11] Y. Ding, W. Zhang, B. Sun, X. Mo, J. Wu, Cyclic freeze-thaw grinding to decellularize meniscus for fabricating porous, elastic scaffolds, J. Biomed. Mater. Res. A 110 (11) (2022) 1824–1839.
[12] R. Zheng, D. Song, Y. Ding, B. Sun, C. Lu, X. Mo, H. Xu, Y. Liu, J. Wu, A comparative study on various cell sources for constructing tissue-engineered meniscus, Front. Bioeng. Biotechnol. 11 (2023) 1128762.
[13] T.J. Keane, S.F. Badylak, The host response to allogeneic and xenogeneic biological scaffold materials, J. Tissue Eng. Regen. Med. 9 (5) (2015) 504–511.
[14] S.F. Badylak, Decellularized allogeneic and xenogeneic tissue as a bioscaffold for regenerative medicine: factors that influence the host response, Ann. Biomed. Eng. 42 (7) (2014) 1517–1527.
[15] Y. Qu, B. Chu, J. Li, H. Deng, T. Niu, Z. Qian, Macrophage-Biomimetic Nanoplatform-Based Therapy for Inflammation-Associated Diseases, Small Methods 8 (7) (2023).
[16] R. Klopfleisch, Macrophage reaction against biomaterials in the mouse model - Phenotypes, functions and markers, Acta Biomater. 43 (2016) 3–13.
[17] D. Gvaramia, J. Kern, Y. Jakob, H. Tritschler, R.E. Brenner, R. Breiter, J. Kzhyshkowska, N. Rotter, Modulation of the inflammatory response to decellularized collagen matrix for cartilage regeneration, J. Biomed. Mater. Res. A 110 (5) (2022) 1021–1035.
[18] P. Abraham, K. I, K. D, Nitro-arginine methyl ester, a non-selective inhibitor of nitric oxide synthase reduces ibuprofen-induced gastric mucosal injury in the rat, Dig. Dis. Sci. 50 (9) (2005) 1632–1640.
[19] P. McGettigan, D. Henry, Use of non-steroidal anti-inflammatory drugs that elevate cardiovascular risk: an examination of sales and essential medicines lists in low-, middle-, and high-income countries, PLoS. Med. 10 (2) (2013) e1001388.
[20] P. Li, L. Ruan, G. Jiang, Y. Sun, R. Wang, X. Gao, K.E. Yunusov, U.E. Aharodnikau, S.O. Solomevich, Design of 3D polycaprolactone/epsilon-polylysine-modified

chitosan fibrous scaffolds with incorporation of bioactive factors for accelerating wound healing, Acta Biomater. 152 (2022) 197–209.
[21] S.R. Balusamy, S. Rahimi, J. Sukweenadhi, S. Sunderraj, R. Shanmugam, L. Thangavelu, I. Mijakovic, H. Perumalsamy, Chitosan, chitosan nanoparticles and modified chitosan biomaterials, a potential tool to combat salinity stress in plants, Carbohydr. Polym. 284 (2022) 119189.
[22] J. Wu, C. Huang, W. Liu, A. Yin, W. Chen, C. He, H. Wang, S. Liu, C. Fan, G. L. Bowlin, X. Mo, Cell infiltration and vascularization in porous nanoyarn scaffolds prepared by dynamic liquid electrospinning, J. Biomed. Nanotechnol. 10 (4) (2014) 603–614.
[23] Z. Yuan, D. Sheng, L. Jiang, M. Shafiq, A.U.R. Khan, R. Hashim, Y. Chen, B. Li, X. Xie, J. Chen, Y. Morsi, X. Mo, S. Chen, Vascular Endothelial Growth Factor-Capturing Aligned Electrospun Polycaprolactone/Gelatin Nanofibers Promote Patellar Ligament Regeneration, Acta Biomater. 140 (2022) 233–246.
[24] W. Chen, S. Chen, Y. Morsi, H. El-Hamshary, M. El-Newhy, C. Fan, X. Mo, Superabsorbent 3D Scaffold Based on Electrospun Nanofibers for Cartilage Tissue Engineering, ACS. Appl. Mater. Interfaces 8 (37) (2016) 24415–24425.
[25] Z. Yuan, Y. Ren, M. Shafiq, Y. Chen, H. Tang, B. Li, M. El-Newehy, H. El-Hamshary, Y. Morsi, H. Zheng, X. Mo, Converging 3D Printing and Electrospinning: Effect of Poly(l-lactide)/Gelatin Based Short Nanofibers Aerogels on Tracheal Regeneration, Macromol. Biosci. 22 (1) (2021) e2100342.
[26] X. Yu, G. Shen, J. Yan, W. Guo, Z. Yuan, J. Cui, Y. Shen, P. Cai, Y. Chen, M.T. Ngai, M. El-Newehy, H. El-Hamshary, B. Sun, J. Li, X. Mo, Induction of macrophage polarization by electrospun nano-yarn containing naproxen sodium to promote tendon repair, Appl. Mater. Today 36 (2024) 102070.
[27] P. Cai, C. Li, Y. Ding, H. Lu, X. Yu, J. Cui, F. Yu, H. Wang, J. Wu, M. El-Newehy, M. M. Abdulhameed, L. Song, X. Mo, B. Sun, Elastic 3D-printed nanofibers composite scaffold for bone tissue engineering, ACS Appl. Mater. Interfaces 15 (47) (2023) 54280–54293.
[28] M. Liu, W. Zhang, Z. Chen, Y. Ding, B. Sun, H. Wang, X. Mo, J. Wu, Mechanisms of magnesium oxide-incorporated electrospun membrane modulating inflammation and accelerating wound healing, J. Biomed. Mater. Res. A 111 (1) (2023) 132–151.
[29] L. Zhu, S. Chen, K. Liu, W. Wen, L. Lu, S. Ding, C. Zhou, B. Luo, 3D poly (L-lactide)/chitosan micro/nano fibrous scaffolds functionalized with quercetin-polydopamine for enhanced osteogenic and anti-inflammatory activities, Chem. Eng. J. 391 (2020) 123524.
[30] Z. Yuan, L. Zhang, S. Jiang, M. Shafiq, Y. Cai, Y. Chen, J. Song, X. Yu, H. Ijima, Y. Xu, X. Mo, Anti-inflammatory, antibacterial, and antioxidative bioactive glass-based nanofibrous dressing enables scarless wound healing, Smart. Mater. Med. 4 (2023) 407–426.
[31] M. Brittberg, C.S. Winalski, Evaluation of cartilage injuries and repair, J. Bone Joint Surg. Am. 85-A (Suppl 2) (2003) 58–69.
[32] D.M. Giraldo-Gomez, S.J. Garcia-Lopez, L. Tamay-de-Dios, R. Sanchez-Sanchez, J. Villalba-Caloca, A. Sotres-Vega, M.L. Del Prado-Audelo, K.K. Gomez-Lizarraga, D. Garciadiego-Cazares, M.C. Pina-Barba, Fast cyclical-decellularized trachea as a natural 3D scaffold for organ engineering, Mater. Sci. Eng. C. Mater. Biol. Appl. 105 (2019) 110142.
[33] M. Liu, X. Wang, H. Li, C. Xia, Z. Liu, J. Liu, A. Yin, X. Lou, H. Wang, X. Mo, J. Wu, Magnesium oxide-incorporated electrospun membranes inhibit bacterial infections and promote the healing process of infected wounds, J. Mater. Chem. B 9 (17) (2021) 3727–3744.
[34] J.C. McNelis, J.M. Olefsky, Macrophages, immunity, and metabolic disease, Immunity. 41 (1) (2014) 36–48.
[35] N. Mehrban, C.Pineda Molina, L.M. Quijano, J. Bowen, S.A. Johnson, J. Bartolacci, J.T. Chang, D.A. Scott, D.N. Woolfson, M.A. Birchall, S.F. Badylak, Host macrophage response to injectable hydrogels derived from ECM and alpha-helical peptides, Acta Biomater. 111 (2020) 141–152.
[36] M. Zhu, W. Li, X. Dong, X. Yuan, A.C. Midgley, H. Chang, Y. Wang, H. Wang, K. Wang, P.X. Ma, H. Wang, D. Kong, In vivo engineered extracellular matrix scaffolds with instructive niches for oriented tissue regeneration, Nat. Commun. 10 (1) (2019) 4620.
[37] X. He, W. Li, S. Liu, Y. Li, Y. Chen, N. Dan, W. Dan, M. Zhu, Fabrication of high-strength, flexible, porous collagen-based scaffolds to promote tissue regeneration, Mater. Today Bio 16 (2022) 100376.
[38] A. Kara, S. Koçtürk, G. Bilici, H. Havitcioglu, Development of biological meniscus scaffold: Decellularization method and recellularization with meniscal cell population derived from mesenchymal stem cells, J. Biomater. Appl. 35 (9) (2021) 1192–1207.
[39] C.A. Murphy, G.M. Cunniffe, A.K. Garg, M.N. Collins, Regional dependency of bovine meniscus biomechanics on the internal structure and glycosaminoglycan content, J. Mech. Behav. Biomed. Mater. 94 (2019) 186–192.
[40] A. Esmaeili, E. Biazar, M. Ebrahimi, S. Heidari Keshel, B. Kheilnezhad, F. Saeedi Landi, Acellular fish skin for wound healing, Int. Wound J. 20 (7) (2023) 2924–2941.
[41] Y. Wang, F. Liu, N. Wang, G. Yue, X. Wang, B. Cai, Y. Hao, Y. Li, F. Guo, Z. Zhang, S. Wang, M. Guo, L. Kong, Y. Zhao, L. Jiang, Y. Zhao, Bioinspired stretchable helical nanofiber yarn scaffold for locomotive tissue dynamic regeneration, Matter 5 (12) (2022) 4480–4501.
[42] X. Deng, M. Gould, M.A. Ali, Fabrication and characterisation of melt-extruded chitosan/keratin/PCL/PEG drug-eluting sutures designed for wound healing, Mater. Sci. Eng. C Mater. Biol. Appl. 120 (2021) 111696.
[43] R. Zhang, S.J. Chang, Y. Jing, L. Wang, C.J. Chen, J.T. Liu, Application of chitosan with different molecular weights in cartilage tissue engineering, Carbohydr. Polym. 314 (2023) 120890.
[44] M.A. Shamekhi, A. Rabiee, H. Mirzadeh, H. Mahdavi, D. Mohebbi-Kalhori, M. Baghaban Eslaminejad, Fabrication and characterization of hydrothermal cross-linked chitosan porous scaffolds for cartilage tissue engineering applications, Mater. Sci. Eng. C Mater. Biol. Appl. 80 (2017) 532–542.
[45] A. Abarrategi, Y. Lópiz-Morales, V. Ramos, A. Civantos, L. López-Durán, F. Marco, J.L. López-Lacomba, Chitosan scaffolds for osteochondral tissue regeneration, J. Biomed. Mater. Res. A 95 (4) (2010) 1132–1141.
[46] A. Pemmari, L. Tuure, M. Hämäläinen, T. Leppänen, T. Moilanen, E. Moilanen, Effects of ibuprofen on gene expression in chondrocytes from patients with osteoarthritis as determined by RNA-Seq, RMD. Open. 7 (3) (2021) e001657.
[47] L. Moradi, M. Vasei, M.M. Dehghan, M. Majidi, S.Farzad Mohajeri, S. Bonakdar, Regeneration of meniscus tissue using adipose mesenchymal stem cells-chondrocytes co-culture on a hybrid scaffold: In vivo study, Biomaterials 126 (2017) 18–30.
[48] P. Thomas, C. von der Helm, C. Schopf, F. Mazoochian, L. Frommelt, H. Gollwitzer, J. Schneider, M. Flaig, V. Krenn, B. Thomas, B. Summer, Patients with Intolerance Reactions to Total Knee Replacement: Combined Assessment of Allergy Diagnostics, Periprosthetic Histology, and Peri-implant Cytokine Expression Pattern, Biomed. Res. Int. 2015 (2015) 1–9.
[49] Y. Li, C. Hu, B. Hu, J. Tian, G. Zhao, C. Cai, Y. Li, Z. Sun, S. Wang, S. Pang, R. Bao, Z. Tao, H. Chen, J. Wu, S. Liu, Sustained Release of Dicumarol via Novel Grafted Polymer in Electrospun Nanofiber Membrane for Treatment of Peritendinous Adhesion, Adv. Healthc. Mater. 12 (15) (2023) e2203078.
[50] P. Lepetsos, A.G. Papavassiliou, ROS/oxidative stress signaling in osteoarthritis, Biochim. Biophys. Acta 1862 (4) (2016) 576–591.
[51] S. Carnevale, I. Di Ceglie, G. Grieco, A. Rigatelli, E. Bonavita, S. Jaillon, Neutrophil diversity in inflammation and cancer, Front. Immunol. 14 (2023) 1180810.
[52] D. Zhang, Q. Chen, C. Shi, M. Chen, K. Ma, J. Wan, R. Liu, Dealing with the Foreign-Body Response to Implanted Biomaterials: Strategies and Applications of New Materials, Adv. Funct. Mater. 31 (6) (2020) 2007226.
[53] Y. Sun, D.R. Mauerhan, J.S. Kneisl, H. James Norton, N. Zinchenko, J. Ingram, E. N. Hanley Jr., H.E. Gruber, Histological examination of collagen and proteoglycan changes in osteoarthritic menisci, Open Rheumatol. J. 6 (2012) 24–32.
[54] G. Zhong, J. Yao, X. Huang, Y. Luo, M. Wang, J. Han, F. Chen, Y. Yu, Injectable ECM hydrogel for delivery of BMSCs enabled full-thickness meniscus repair in an orthotopic rat model, Bioact. Mater. 5 (4) (2020) 871–879.